NASA
Technical
Paper
2327

August 1984



# Results of the First Complete Static Calibration of the RSRA Rotor-Load-Measurement System

C. W. Acree, Jr.



NASA

**NASA Technical Paper 2327**

1984

# Results of the First Complete Static Calibration of the RSRA Rotor-Load-Measurement System

C. W. Acree, Jr.

*Ames Research Center*
*Moffett Field, California*

National Aeronautics and Space Administration

**Scientific and Technical Information Branch**

## SYMBOLS AND CONSTANTS

| | |
|---|---|
| $I'_{TX}, I'_{TY}, I'_{TZ}$ | moments of inertia, not fully corrected for engine mass |
| $L_{I_A}, M_{I_A}, N_{I_A}$ | inertial loads caused by rotational accelerations of the transmission |
| $L_{I_G}, M_{I_G}, N_{I_G}$ | inertial loads caused by precessional moments of the transmission gears |
| $L_{I_{QE}}$ | roll moment caused by engine output torque |
| $L_{I_{QT}}, N_{I_{QT}}$ | roll and yaw moments caused by tail-rotor drive-shaft reaction torque |
| $m'_T$ | transmission mass not fully corrected for engine mass |
| $p,q,r$ | rotational rates in each direction (roll, pitch, and yaw, respectively) |
| $\dot{p},\dot{q},\dot{r}$ | rotational accelerations in each direction |
| $QE$ | engine output torque |
| $QT$ | tail-rotor drive-shaft torque |
| $T_I$ | tail-rotor inertial load (thrust, positive into the tail pylon) |
| $\dot{u},\dot{v},\dot{w}$ | linear accelerations in each direction (longitudinal, lateral, and vertical, respectively) |
| $\dot{u}_A, \dot{v}_A, \dot{w}_A$ | linear accelerations measured by accelerometers |
| $\dot{u}_T, \dot{v}_T, \dot{w}_T$ | linear accelerations referenced to the transmission center of gravity |
| $\dot{v}_{TR}$ | lateral acceleration of the tail rotor gearbox |
| $X,Y,Z,L,M,N$ | individual load components (fig. 3) |
| $X_{I_A}, Y_{I_A}, Z_{I_A}$ | inertial loads caused by linear accelerations of the transmission |
| $X_{I_{\dot{q}}}, M_{I_{\dot{q}}}$ | inertial force and moment (longitudinal and pitch) caused by rotational acceleration in pitch |
| $X_{IR}, Y_{IR}, Z_{IR}, L_{IR}, M_{IR}, N_{IR}$ | total inertial loads in rotor-head axes (individual components of $\vec{F}_{IR}$) |
| $X_{IT}, Y_{IT}, Z_{IT}, L_{IT}, M_{IT}, N_{IT}$ | total inertial loads in transmission center-of-gravity axes (individual components of $\vec{F}_{IT}$) |
| $X_{I_{\dot{u}}}, M_{I_{\dot{u}}}$ | inertial force and moment casued by linear longitudinal acceleration |
| $Y_{I_E}, L_{I_E}$ | inertial side-force and roll moment caused by engine precessional moment |

| | |
|---|---|
| $\theta$ | aircraft pitch angle |
| $\phi$ | aircraft roll angle |

Matrix and Vector Symbols:

| | |
|---|---|
| $\vec{A}_R$ | aircraft acceleration vector in rotor-head axes |
| $\vec{A}_T$ | acceleration vector in transmission center-of-gravity axes |
| $\vec{B}$ | regression vector of load intercepts |
| $C$ | calibration matrix |
| $C_E$ | error propagation matrix |
| $\vec{D}$ | calibration tare vector |
| $\vec{F}_A$ | applied calibration load vector |
| $\vec{F}_E$ | rotor-load error variance vector |
| $\vec{F}_{IR}$ | inertial load vector in rotor-head axes |
| $\vec{F}_{IT}$ | inertial load vector in transmission center-of-gravity axes |
| $\vec{F}_L$ | total load vector measured by load cells |
| $\vec{F}_R$ | total rotor load vector in rotor-head axes |
| $\vec{L}$ | load-cell output vector |
| $\vec{L}_E$ | load-cell error variance vector |
| $\vec{L}_M$ | load-cell output vector measured during calibration |
| $M_R$ | inertial loads matrix in rotor-head axes |
| $M_T$ | inertial loads matrix in transmission center-of-gravity axes |
| $S$ | regression coefficient matrix |
| $T_T$ | transformation matrix to convert from transmission center-of-gravity axes to rotor-head axes |

Constants:

| | |
|---|---|
| $d_1$ | moment arm (fig. B1) 1.424 ft |
| $d_2$ | moment arm (fig. B1) 4.324 ft |

| | |
|---|---|
| $d_3, d_4$ | longitudinal and vertical distances from accelerometer to tail rotor (fig. B2), 36.75 and 3.00 ft, respectively |
| $d_X, d_Y, d_Z$ | distance from accelerometer to transmission center of gravity: longitudinal, −2.6 in.; lateral, −7.0 in.; vertical, +43 in., respectively |
| $g$ | gravity, 32.17 ft/sec$^2$ |
| $H_E$ | engine moment of momentum along turbine shaft, 374.9 ft-lb-sec |
| $H_G$ | transmission gear vertical moment of momentum, −1,836 ft-lb-sec at 203 rpm |
| $I_{TX}$ | transmission roll moment of inertia, 323.2 ft-lb-sec$^2$ |
| $I_{TY}$ | transmission pitch moment of inertia, 392.7 ft-lb-sec$^2$ |
| $I_{TZ}$ | transmission yaw moment of inertia, 174.8 ft-lb-sec$^2$ |
| $m_{TR}$ | mass of tail-rotor gearbox, 206 lb (6.41 slugs) |
| $m_{TX}$ | transmission longitudinal inertia, 4,069 lb (126.5 slugs) |
| $m_{TY}$ | transmission lateral inertia, 3,486 lb (108.3 slugs) |
| $m_{TZ}$ | transmission vertical inertia, 3,486 lb (108.3 slugs) |
| $\Delta m_E$ | additional engine mass in the longitudinal direction, 583.2 lb (18.13 slugs) |
| $\alpha$ | angle of intersection of transmission main output shaft with main-engine input shafts, 4° total |
| $\beta$ | angle of intersection of transmission main output shaft with tail-rotor drive shaft, 8.13° total |

Notes: (1) All moment arms, inertias, and momenta (except engines) are in aircraft body axes aligned to the aircraft waterline and aircraft vertical. (2) The rotor-head reference center is located at XSTA 300.00 (in.); YBL 0.00; ZWL 302.00. (3) The transmission center of gravity is located at XSTA 298.90 (in.); YBL 0.48; ZWL 283.67.

# RESULTS OF THE FIRST COMPLETE STATIC CALIBRATION OF THE RSRA ROTOR-LOAD-MEASUREMENT SYSTEM

C. W. Acree, Jr.

Ames Research Center

## SUMMARY

The compound Rotor Systems Research Aircraft (RSRA) is designed to make high-accuracy, simultaneous measurements of all rotor forces and moments in flight. Physical calibration of the rotor force- and moment-measurement system when installed in the aircraft is required to account for known errors and to ensure that measurement-system accuracy is traceable to the National Bureau of Standards. The first static calibration and associated analysis have been completed with good results. Hysteresis was a potential cause of static calibration errors, but was found to be negligible in flight compared to full-scale loads, and analytical methods have been devised to eliminate hysteresis effects on calibration data. Flight tests confirmed that the calibrated rotor-load-measurement system performs as expected in flight and that it can dependably make direct measurements of fuselage vertical drag in hover.

## INTRODUCTION

Measurement of the forces and moments generated by a helicopter rotor in flight is a key research requirement of the Rotor Systems Research Aircraft (RSRA). The RSRA compound helicopter has a complete helicopter rotor system, as well as an independent wing and a fan-jet propulsion system, allowing an expanded flight envelope for research. This gives the RSRA unique capabilities for testing rotor systems. The RSRA was specifically designed to make high-accuracy, simultaneous measurements of total rotor and wing forces and moments. Figure 1 is an exploded view of the compound RSRA, in which the measurement systems are highlighted. The RSRA and its measurement systems were designed and built by Sikorsky Aircraft.

The load-measurement systems of the compound RSRA have all been calibrated for static loads, traceable to the National Bureau of Standards. During the summer of 1981, a series of flights was made without the wing and auxiliary propulsion engines to allow measurement of vertical drag in hover. These flight tests were reported in a separate paper by Flemming and Erickson (ref. 1). Because hover research is of greatest current interest, this paper will focus primarily on the measurement of rotor loads in hover. The hover flight tests were also used to test the assumption that measurement-system hysteresis, although present during static calibration, is negligible in flight.

General descriptions of the compound RSRA and its sister aircraft, which has a different measurement system not covered here, are given by Burks (ref. 2), who also outlines the calibration process and analysis and presents preliminary results. The present paper gives complete results for the main-rotor load-measurement system and develops the following topics in greater detail: (1) physical calibration of the rotor-load-measurement system; (2) analysis of calibration data; (3) corrections for known error sources, including inertial-effects analysis and aircraft data-system calibration; (4) summary of all calibration and load-measurement errors; and (5) flight-test validation of predicted performance. It also includes a brief discussion of the calibration of the tail rotor, and describes desirable improvements to the aircraft and its calibration suggested by the results of the calibration efforts reported here. This report, which is based on an

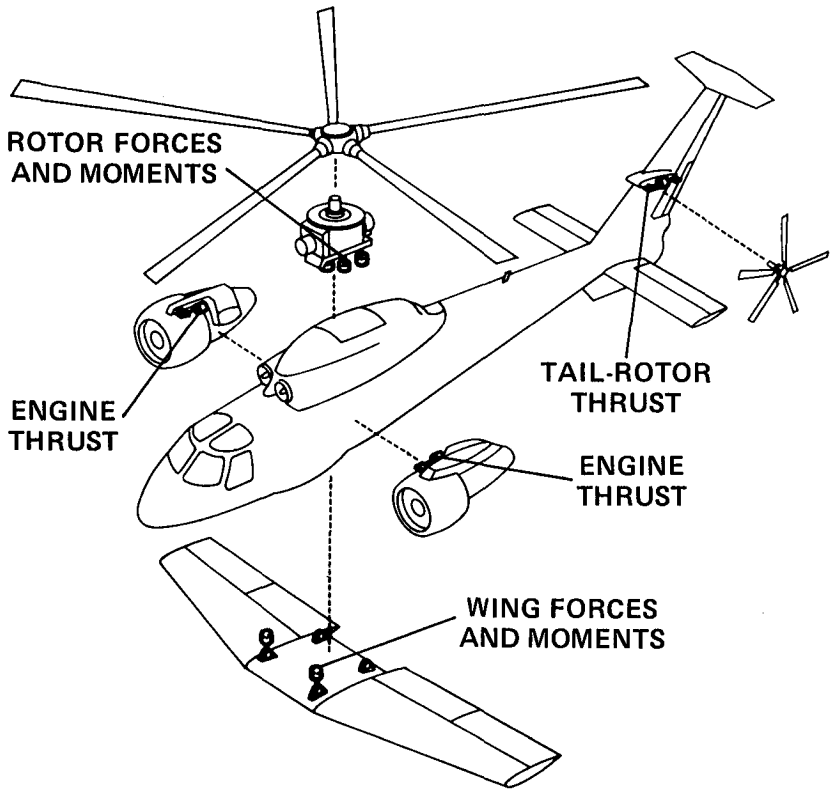


Figure 1.– RSRA load-measurement systems.

earlier paper by the author (ref. 3), includes four appendixes that present detailed discussions of error predictions, inertial-effects calculations, and regression results.

## PHYSICAL CALIBRATION OF THE ROTOR-LOAD-MEASUREMENT SYSTEM

The design of the rotor-load-measurement system is such that a calibration of the full system is required when it is installed in the aircraft. Important insights into the system's behavior can be obtained by examining the raw data before making numerical analyses.

### Description of Aircraft Systems and Calibration Method

Figure 2 shows the rotor-load-measurement system used on the compound version of the RSRA. Seven load cells connect the transmission base-plate to the airframe in an arrangement roughly analogous to that of a wind-tunnel balance. The resulting rotor-balance system can simultaneously measure multiple combinations of forces and moments on the rotor within the limits listed in table 1; an axis system referenced to the intersection of the center of the rotor shaft and the plane of the flapping hinges is used in the table. The axes are labeled as shown in figure 3.

Fail-safe features are emphasized in the design, at the expense of ultimate possible accuracy. Load cells are selected for fatigue strength and are arranged in a parallel-redundant layout. Redundant links, which are designed to be unloaded throughout the flight envelope, would take up loads if a load cell should fail.

If the airframe were perfectly rigid, measurement accuracy, in terms of expected root-mean-square (rms) errors, would be limited primarily by the load cells and the geometry of the measurement system. The equivalent measurement rms errors based on this assumption are listed in table 1 (column 3, Predicted aircraft accuracy) as percentages of full-scale loads. However, structural flexibility in the real aircraft changes the load distributions among the load cells, causing interactions (crosstalk) and errors in sensitivity. Accumulated manufacturing and rigging errors accentuate the problem. The aircraft data system also contributes errors. If the individual load-cell readings are to be correctly transformed into equivalent rotor loads, the load-measurement system must be calibrated as an assembled unit when installed in the aircraft itself.

Detailed descriptions of the static-calibration equipment and procedures are given by Acree et al. (ref. 4). A summary of important features is given here. Figure 4 is a schematic representation of the static-calibration method. A special calibration fixture replaced the rotor head, and the airframe was tied down by the landing-gear mounting lugs. Hydraulic cylinders applied static loads through cables and pulleys to the rotor-head fixture, except for lift; a solid rod and walking beam were used for lift to carry the higher forces required. High-accuracy calibration reference load cells connected the cables and rods to the rotor-head fixture. Weight and airworthiness were not important here, so the rotor-head fixture, tie-down restraints, and hydraulic-cylinder supports and connecting framework were made extra strong for high stiffness; the rotor-head fixture geometry allowed each calibration load cell to measure a single applied load directly in the rotor-head reference axis system.

A set of tilt sensors and adjustable aircraft restraints ensured that the rotor shaft remained aligned perpendicular to the cables and parallel to the vertical load rod. Deflections no greater than 0.5° were allowed. The tie-down restraints were adjusted as necessary to maintain proper alignment. Applied-load data were trigonometrically corrected, using tilt-sensor angular data.

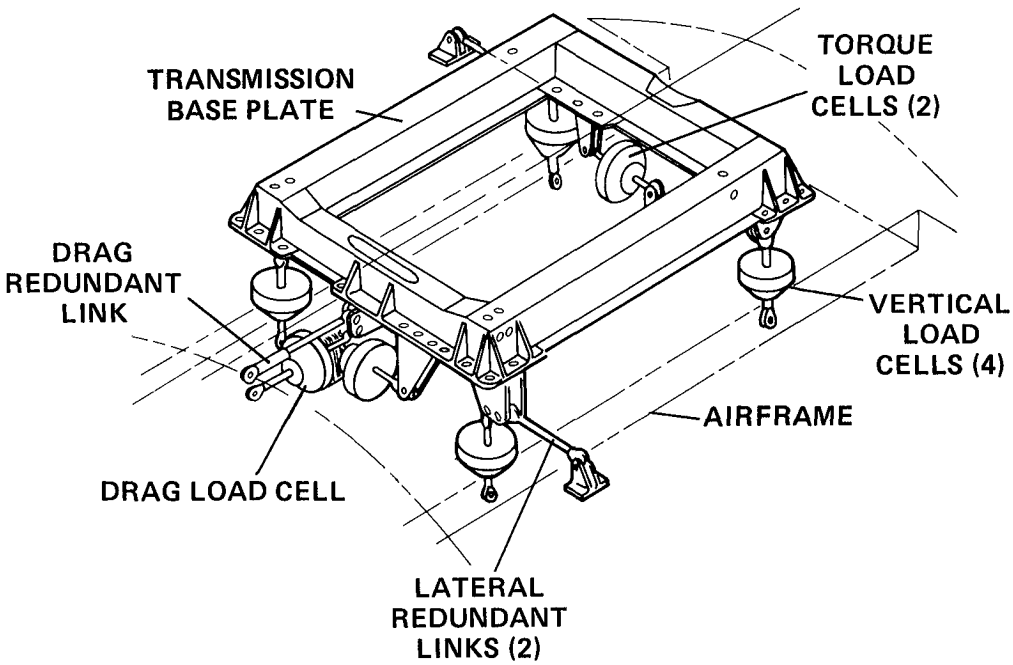


Figure 2.– Rotor-load-measurement system.

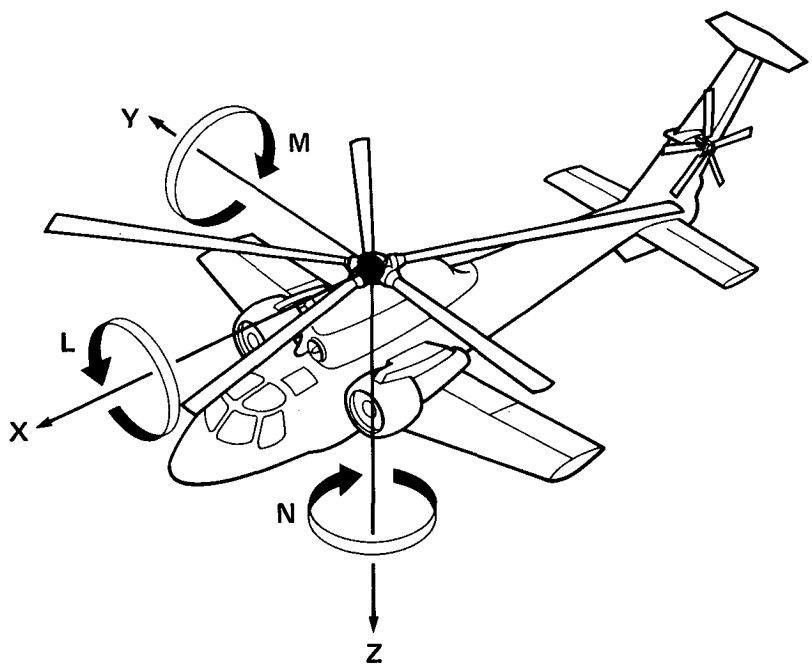


Figure 3.– RSRA rotor calibration axis system.

TABLE 1.– RSRA STATIC-CALIBRATION FACILITY CAPABILITIES

| Rotor-head axis | | Full-scale loads (S-61 rotor) | Predicted aircraft accuracy,[a] % | Facility calibration accuracy,[a] % |
|---|---|---|---|---|
| Longitudinal | $X$ | ±8,620 lb | 0.24 | 0.20 |
| Lateral | $Y$ | ±5,420 lb | 1.6 | .14 |
| Vertical | $Z$ | 48,000 lb | .25 | .11 |
| Rolling moment | $L$ | ±16,650 ft-lb | 1.6 | .19 |
| Pitching moment | $M$ | +25,000 ft-lb | .95 | .27 |
| | | -16,650 ft-lb | 1.4 | .43 |
| Rotor torque | $N$ | 58,200 ft-lb | .26 | .16 |

[a]Root-mean-square error as a percentage of full-scale load.

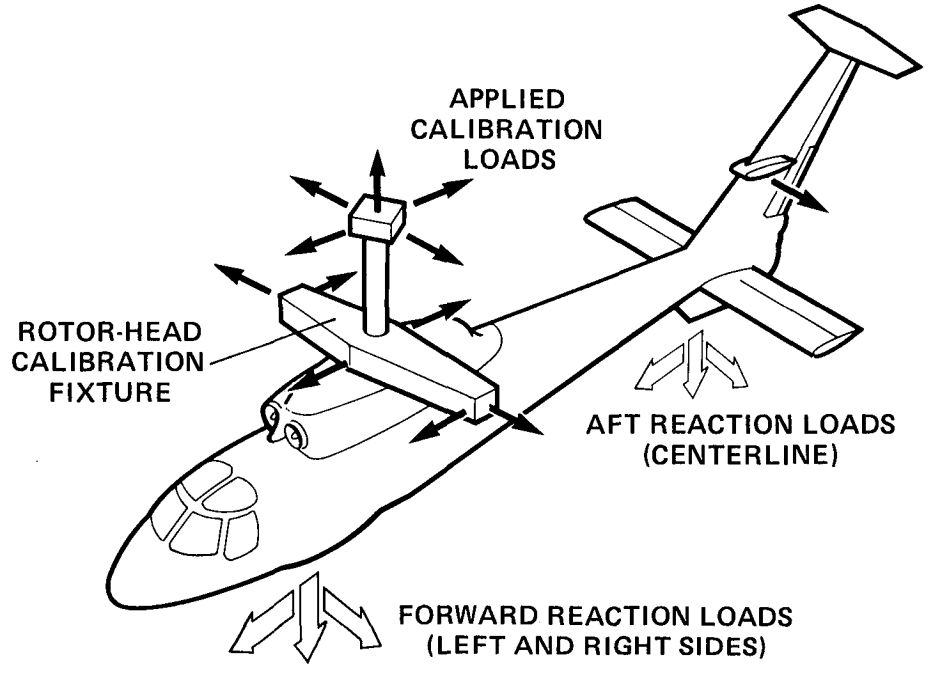


Figure 4.– Method of applying static rotor calibration loads to the RSRA.

During calibration, all aircraft and calibration load cells were wired to matched digital voltmeters, and all calibration data were recorded by hand. Before calibration, all load cells were individually calibrated with their meters, using a secondary standard load cell that was calibrated using equipment traceable to the National Bureau of Standards. Such calibrations of the reference load cells and meters determined the facility accuracies given in table 1. These accuracies are slightly better than the best possible aircraft accuracies; as will be shown, facility accuracies are much better than actual aircraft measurement-system accuracies, so that the calibration is valid overall. (See appendix A for a discussion of different predictions of system accuracy.) The aircraft data system used for recording flight data was calibrated separately, as will be described later.

Some of the calibration equipment and procedures were developed concurrently with the calibration of the aircraft. This forced several compromises to be made, notably, lack of refinement of the calibration data sets and deletion of data replications. The overall success of the calibration in spite of such restrictions gave confidence that the basic approach is sound.

## Physical Implications of Raw Data

Before covering the calibration data analysis in detail, it is worthwhile to discuss qualitatively a few examples of the raw data to illustrate important system behavior. Figure 5 shows the output of the drag (longitudinal) aircraft load cell versus applied $X$ (longitudinal) load. The negative slope was due to the electrical output sign convention of the load cell. Saturation above about 5,000 lb is obvious; it was due to premature tightening of the drag redundant link.

When torque and lateral loads were applied, saturation also occurred in the two lateral aircraft load cells because of the lateral redundant links. Saturation in any axis was expected to occur in flight only in regions of the maneuver envelope of low research priority, so data in the saturated regions were deleted to avoid introducing slope errors into the numerical analysis.

Figure 5 also shows hysteresis in the load-cell output, which reflects typical measurement-system behavior. The same data, in the unsaturated range, are replotted in figure 6 as deviations from a straight line through the center of the hysteresis band, thus emphasizing the hysteresis errors. All load cells showed hysteresis, to varying degrees, under all applied loads. It is strongly suspected that this is a result of excessive friction of the spherical bearings in the rod ends which connect the aircraft load cells to the transmission and airframe. Independent tests of sample rod-ends disclosed friction levels sufficient to account for the hysteresis. Since there are six possible applied loads, each potentially causing hysteresis errors in each of six output axes, there is in effect a 12-dimensional error space, of which only a two-dimensional slice is shown in figure 6. A key assumption of the calibration is that the dithering effect of rotor vibrations collapses the hysteresis bands of each axis in flight; this assumption was verified by flight tests (discussed in the Flight-Test Validation section).

Also noticeable in figure 6 are "zero-crossing errors": unusually large deviations in the errors near zero applied load. Only tension forces can be applied through cables, so to reverse applied load direction, different load cells, cables, and hydraulic cylinders must be used for the same axis. This prevented smooth, continuous application of loads across zero during calibration. The initial data point taken after a change in direction often deviated excessively from neighboring data points; such initial data points were deleted on the grounds that their deviations were results of the calibration process and not representative of true behavior in flight. Preliminary results of the calibration of the second RSRA (ref. 5) support this assumption.

A similar phenomenon, skewed data, is shown in figure 7. Although fairly straight with equal slopes, the positive and negative data were skewed away from each other and did not properly intersect at zero load. It

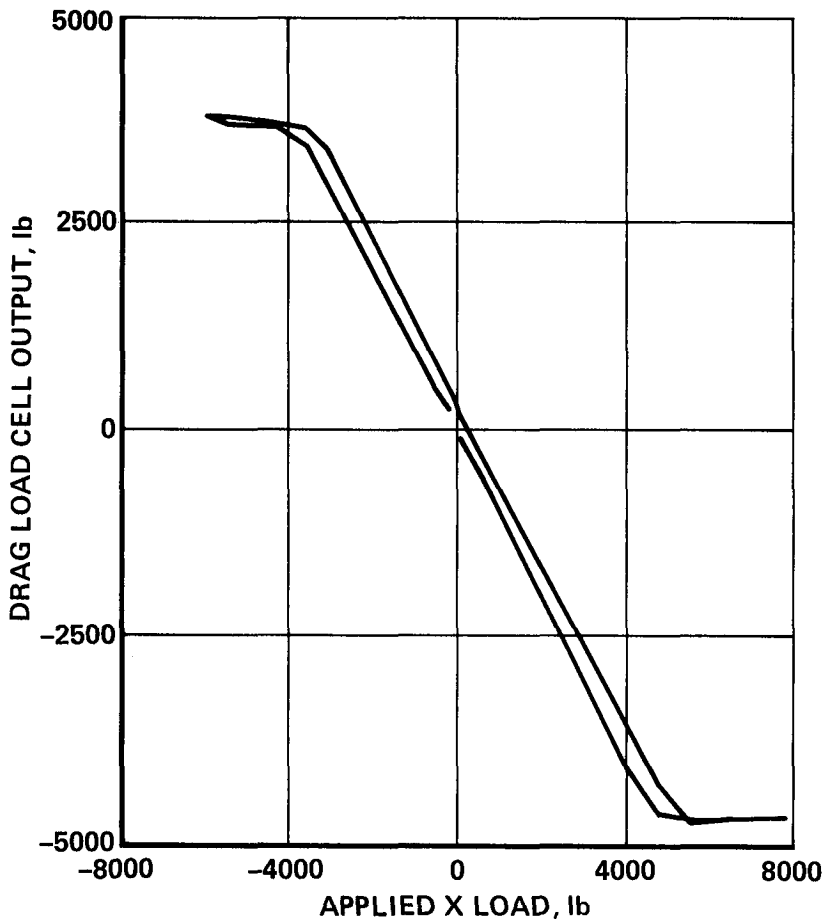


Figure 5.– Drag load-cell output versus applied longitudinal calibration load.

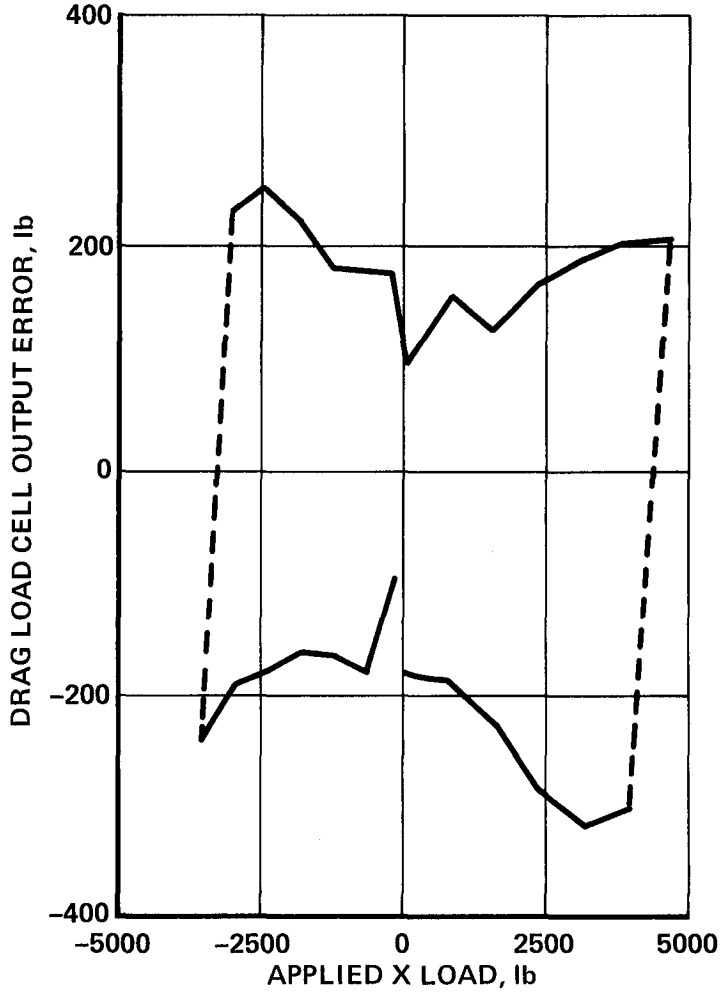


Figure 6.– Deviations from linear slope of drag load-cell output for applied longitudinal calibration load (saturated data deleted).

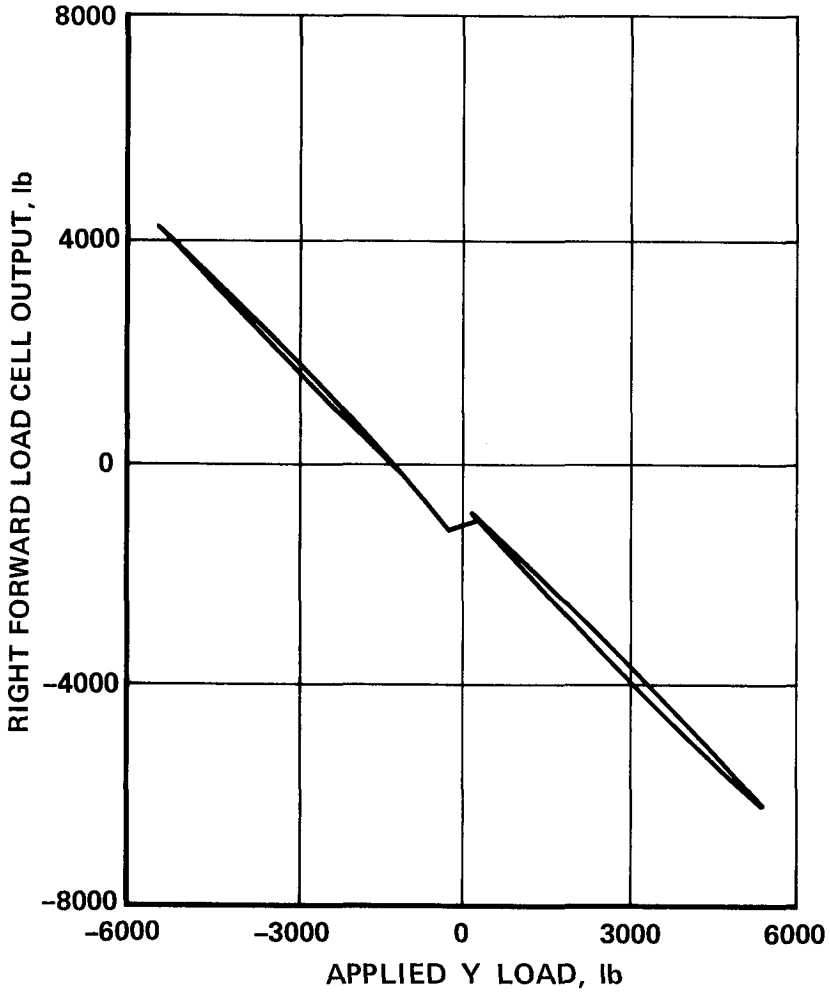


Figure 7.— Right forward vertical load-cell output versus applied lateral load.

was not always possible to avoid disturbing the aircraft between changes of load direction, especially if the aircraft had to be realigned to keep within the 0.5° deflection limit. Again, this was a result of the calibration process and was not evident in flight; such skewed data were accordingly adjusted to get equal vertical-axis intercepts. Positive and negative data were given equal and opposite bias shifts to eliminate the skew while retaining the original slopes, overall biases, and relative errors.

## ANALYSIS OF CALIBRATION DATA

An inverse-regression technique was used to analyze the calibration data in order to avoid numerical difficulties. Several different combinations of data were analyzed; the most important results are summarized here.

### Regression Analysis

The desired equation for flight-load measurement is, for each data point,

$$\vec{F}_R = C\vec{L} - M_R\vec{A}_R \tag{1}$$

The data available in flight are load-cell outputs $\vec{L}$ and aircraft accelerations $\vec{A}$; during calibration all quantities except the calibration matrix $C$ are known. The choice of the best $C$-matrix for predicting the true rotor force $\vec{F}_R$ constitutes the bulk of the calibration analysis. All possible linear corrections for load-cell sensitivities, measurement-system geometry, and structural flexibility are included in the $C$-matrix. Calculation of the inertial-effects matrix $M_R$ is discussed separately in the section entitled Inertial Effects, and in greater detail in appendix B.

During calibration, $\vec{F}_R$ was the vector of known applied forces, and $\vec{A}$ was constant at 1 g. A conventional multiple-linear-regression analysis could in principle be used to find $C$ by treating $\vec{F}_R$ as the dependent variable, one axis at a time, and $\vec{L}$ as the vector of independent variables. The elements of each row of $C$ would then be the regression coefficients for one axis. A proper regression analysis adjusts the values of the regression coefficients to minimize the errors in the dependent variable over the full ranges of all independent variables.

Numerical difficulties restricted the use of this method in the case of the RSRA. For example, the four vertical load cells are parallel to each other, as shown in figure 2. The outputs of these load cells were consequently all highly correlated with each other, sometimes leading to ill-conditioned matrices within the regression calculations. Even if the load-cell outputs were different in magnitude and sign, significant statistical correlation was still often present. There was, therefore, an infinite number of linear combinations of vertical load-cell data giving equally good fits to applied vertical loads. This ultimately caused excessive sensitivity of the regression coefficients to very small differences in individual load-cell accuracies and even to numerical round-off errors – clearly an unacceptable situation.

Such numerical problems were avoided in this case by using an inverse regression, where

$$\vec{L}_M = S\vec{F}_A \tag{2}$$

The load-cell outputs $\vec{L}_M$ measured during calibration were then dependent variables, and the applied loads were independent variables. The applied load vector $\vec{F}_A$ was completely under the experimenter's control; through careful choice of applied loads, potentially troublesome correlations could be avoided. Then

the inverse-regression coefficient matrix $S$ could be calculated without difficulty; it was manipulated back into the desired form of $C$ by a pseudoinverse:

$$C = [S^T S]^{-1} S^T \tag{3}$$

A forward-stepwise multiple-linear-regression technique was used; Jennrich (ref. 6) describes the method itself, and Draper and Smith (ref. 7) discuss the rationale for its use. Double-precision computer routines eventually gave acceptable results for direct regressions, but inverse regressions remained the preferred method because of inherently greater numerical reliability. An inverse regression may not give acceptable results if there are significant fundamental nonlinearities, but the data were sufficiently linear that numerical accuracy was the greater problem here.

It is also necessary to account for regression intercepts and calibration tares. The effects of several different sources of bias are lumped together in the regression intercept vector $\vec{B}$: the weight of the transmission, the tare weight of the rotor-head calibration fixture, electronic biases in the load cells, and biases owing to nonlinearities. The transmission weight should cancel the inertial effects term $M_R\vec{A}_R$, except for any modifications to the transmission required for calibration. Load-cell electronic offsets are small, and are the same for flight as during calibration. If there are any nonlinearities in the data, the best linear regression line will not necessarily pass through true zero, adding yet another component to the regression intercepts.

The rotor-head calibration fixture is not the same weight as the rotor head and blades it replaces, and the main engines were detached from the transmission for this calibration. These two differences from normal flight configuration require an explicit tare term $\vec{D}$ to be carried in addition to the regression intercepts. Expanding equation (1) to include intercepts and tares yields

$$\vec{F}_R = C\vec{L} - M_R\vec{A}_R + \vec{B} + \vec{D} \tag{4}$$

An inverse regression calculates load-cell intercepts. To convert to load intercepts $\vec{B}$, the negative of the load-cell intercept vector is premultiplied by the matrix $C$ given in equation (3). Examples of $C$, $\vec{B}$, and $\vec{D}$ are given in appendix C.

## Error Analysis

Figure 8 shows the overall analysis logic. A set of applied calibration loads and resulting load-cell outputs yielded the data used in each multiple linear regression to find a candidate calibration matrix. In principle, the standard errors of the regression could be propagated back through the $C$-matrix to get equivalent calibration errors in the applied-load axis system at the rotor head. This was limited in flexibility, so the errors were calculated by multiplying the load-cell data by the candidate $C$-matrix, then comparing the derived rotor loads with the known calibration loads. This allowed evaluation of load-prediction accuracy in any axis for any arbitrary combination of applied loads, which is not possible with direct propagation of regression standard errors. The inertial effects $M_R\vec{A}_R$ and the tares $\vec{D}$ were constant during calibration and canceled out.

Separating the regression and error-calculation parts of the analysis also made it possible to use different data sets with the same $C$-matrix when calculating errors. By choosing a restricted set of calibration data for the regression, the $C$-matrix could be optimized for a specific flight condition. Then calibration data representing different flight conditions could be multiplied by the candidate $C$-matrix to find errors for each condition. In addition, by calculating errors separately for increasing and decreasing applied loads, errors could be calculated for the case of zero hysteresis in order to estimate better the actual flight behavior of the system.

It is too cumbersome to tabulate all possible errors in each axis caused by all applied loads for each *C*-matrix. The error of greatest interest in a given axis is that caused by a load applied to the same axis. For a well-behaved system, this is the largest error in the measurement axis. These are the errors that are defined throughout this paper as "applied-load errors," tabulated in tables 3 and 4, and in table A1 (appendix A) and table D1 (appendix D). Appendix D also gives measurement errors averaged over all applied loads.

There are four distinguishable classes of error: (1) linear sensitivity and interaction errors, which are eliminated by a properly derived calibration matrix; (2) pure hysteresis errors, which have been shown to be negligible in flight (see later section entitled Flight-Test Validation); (3) nonlinearities, for which this calibration analysis method cannot compensate; and (4) true random errors, which can in principle be eliminated by replication and averaging. (Nonlinear extensions of the method are possible, and will be used in the future if necessary for specific research). The effects of pure hysteresis on the calibration data are removed by finding the mean errors for increasing and decreasing applied loads, making equal and opposite bias adjustments to the data to make both sides of the hysteresis loop have equal means, then recalculating the errors for the adjusted data. Residual slope and interaction errors, nonlinearities, and random errors are still present, as they would be in flight.

If there are several physical sources of errors distributed throughout the load-measurement system, then it may be expected that as the magnitude and direction of the applied load changes, different error mechanisms come into play in different relative degrees. This is the primary reason for doing multiple-load calibrations (described below): the total error may not be equal to simply the sum of all single-load errors. Unfortunately, this also means that it may not be possible to find one set of calibration corrections that is adequate for all load configurations of interest. Even when multiple loads are taken into account, a calibration solution which globally minimizes load-measurement errors may not yield minimum errors for any single, isolated axis. The problem is theoretically solvable only by applying calibration loads in all six axes simultaneously over all full-scale ranges. However, neither the physical calibration nor the calibration analysis is practical for the six-load case.

Significant hysteresis effects compound the problem, and may corrupt even a full six-load calibration. There is, in effect, a six-dimensional hysteresis-error envelope, defined by the hysteresis errors of each of the six output axes. Since there are also six possible applied loads, the hysteresis envelope lies within a 12-dimensional load-error space. The critical assumption is that in flight, with substantial rotor vibration present, the hysteresis envelope is reduced in size (volume) so that it is much smaller than the total load-measurement space; hence, it may be ignored. This is not true during static calibration. It is, in general, impossible to measure perfectly or to control exactly the location of the system within its hysteresis envelope, although points on the boundaries (e.g., single loads) can be determined. As long as the hysteresis-error envelope is small, this is adequate for intended research.

## Calibration-Data Organization

Several major data sets were analyzed; the three major ones – single, double, and triple loads – are summarized in table 2. Single loads were applied in 10% increments up to the full-scale limits given in table 2. Double loads were applied by holding the load of one axis constant at 50% full scale while the other was varied from 0% to 50%. All possible combinations, positive and negative, were applied except for downward $Z$ and negative $N$ (owing to limited research interest) and the combinations $+X+M$, $-X-M$, $+Y-L$, and $-Y+L$ (owing to design limitations of the calibration fixture and framework). Note that since either load of each pair could be held constant while the other was varied, there were twice as many double-load calibration conditions as are shown in table 2 for double loads.

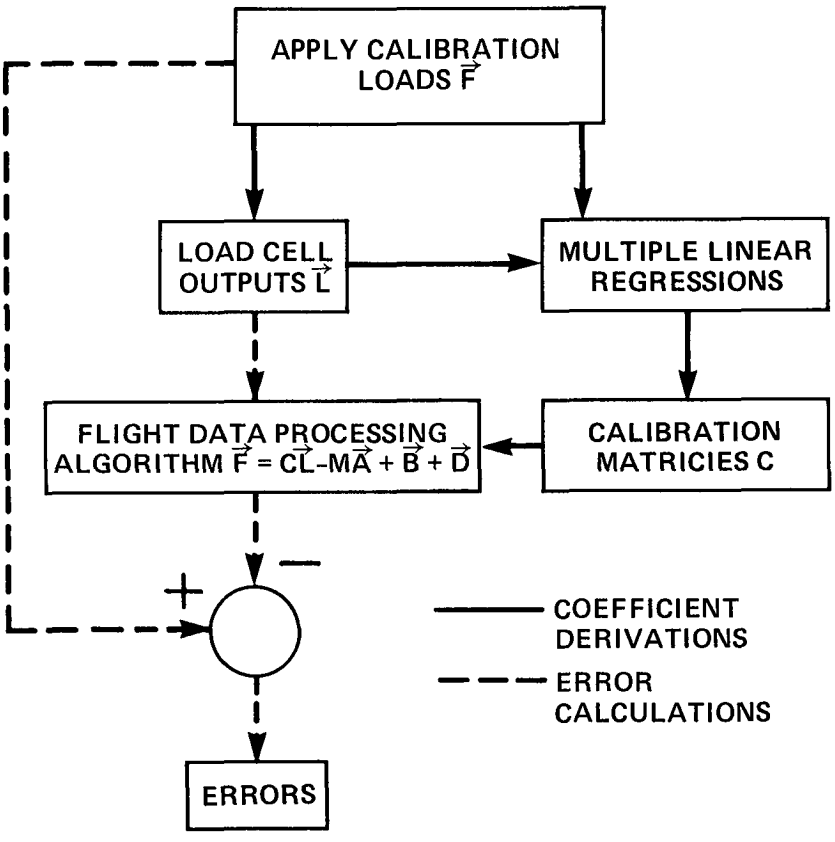


Figure 8.– Flowchart of load-measurement-system calibration data analysis.

TABLE 2.– APPLIED CALIBRATION LOAD COMBINATIONS USED IN REGRESSION ANALYSIS

| Single loads | Maximum magnitudes | Double-load combinations (50% maximum magnitudes) | | | Triple-load combinations (50% maximum magnitudes) | | |
|---|---|---|---|---|---|---|---|
| +*X* | +8,620 lb | +*X*+*Y* | +*Y*−*Z* | −*Z*+*L* | −*Z*+*N*+*X* | −*Z*+*N*+*L* | (−*Z*+*N*) |
| −*X* | −8,620 lb | +*X*−*Y* | −*Y*−*Z* | −*Z*−*L* | −*Z*+*N*−*X* | −*Z*+*N*−*L* | (+*N*−*Z*) |
| | | −*X*+*Y* | | | | | |
| +*Y* | +5,420 lb | −*X*−*Y* | +*Y*+*L* | −*Z*+*M* | −*Z*+*N*+*Y* | −*Z*+*N*+*M* | |
| −*Y* | −5,420 lb | | −*Y*−*L* | −*Z*−*M* | −*Z*+*N*−*Y* | −*Z*+*N*−*M* | |
| | | +*X*−*Z* | | | | | |
| −*Z* | −48,800 lb | −*X*−*Z* | +*Y*+*M* | −*Z*+*N* | | | |
| | | | +*Y*−*M* | | | | |
| +*L* | +16,650 ft-lb | +*X*+*L* | −*Y*+*M* | +*L*+*M* | | | |
| −*L* | −16,650 ft-lb | +*X*−*L* | −*Y*−*M* | +*L*−*M* | | | |
| | | −*X*+*L* | | −*L*+*M* | | | |
| +*M* | +25,000 ft-lb | −*X*−*L* | +*Y*+*N* | −*L*−*M* | | | |
| −*M* | −16,650 ft-lb | | −*Y*+*N* | | | | |
| | | +*X*−*M* | | +*L*+*N* | | | |
| +*N* | +58,200 ft-lb | −*X*+*M* | | −*L*+*N* | | | |
| | | +*X*+*N* | | +*M*+*N* | | | |
| | | −*X*+*N* | | −*M*+*N* | | | |

Triple loads were applied by holding $-Z$ and $+N$ constant at 50% of maximum load, while each other axis in turn was varied over ±50% full-scale range. No loads other than $Z$ and $N$ were held constant for triple-load calibrations. To get a complete data set for a regression analysis, the two $-Z+N$ combinations from the double-load data set were added.

There were 10 single-load cases, 74 (37X2) double-load combinations, and 10 triple-load combinations, or 92 possibilities altogether (counting the $-Z+N$ combinations only once each), as shown in table 2. Since there are seven load cells, there were 644 (7X92) possible subsets of output data. Calibration errors were determined separately for each load axis, so there were in addition 552 (6X92) subsets of calibration-error statistics.

To keep data handling manageable, the regression analysis was performed on complete sets of single-, double-, or triple-load data. That is, the $\vec{F}_A$ vector in equation (2) would include all applied loads in one of the three data sets, and the inverse regression would be performed seven times, once for each load cell in the $\vec{L}_M$ vector. Even larger data sets were constructed by combining the three data major data sets in table 2 in different ways. Several different $C$-matrices were thus derived, and each was used with all of the available data sets to get a wide variety of calibration error estimates for each load axis.

It is impractical to cover more than a few such cases in detail. Summary results for all analyses are given in appendix D. Table 3 summarizes the rms errors for the most important data sets, as detailed in table 2. The numbers given are for errors in the same axis as the applied load, or varied load for multiple loads. For double loads, the errors were averaged over all combinations of varied loads in the error axis with constant loads in other axes. The double-plus-triple-load combined data set is also included for later reference. As was expected, the $C$-matrix derived from any given data set gave lower overall errors than any other $C$-matrix tried on that data set. The errors given for any data set were, therefore, calculated using a calibration matrix derived directly from that same data set. (Exceptions are explicitly noted in appendix D.)

Single loads, although conceptually simple, represent no realistic flight conditions. They are presented in table 3 to show the effects of hysteresis, which is most severe in the $X$ and $N$ axes. Double loads represent no particular flight condition, but their average errors are a reasonable approximation of average system performance over the whole flight envelope. Triple loads were constructed to be equivalent to hover and low-speed flight. For reasons discussed in the next section, the matrix derived from the double-plus-triple-loads data set was chosen for correction of flight data.

Results for the best possible errors are included in the last column of table 3 for comparison. As presented, these numbers for the ideal case are independent of range, so they are valid for the reduced-range multiple loads. Note that some regression errors are less than the predicted best errors. This is due to better-than-specified aircraft load-cell accuracies, and usually occurs in axes in which hysteresis errors are relatively small. For reference, a variety of different predicted errors based on different assumptions is presented in appendix A.

It was decided to forego replications of the calibration data in favor of applying all possible double loads plus selected triple loads. This sacrificed the ability to average out true random errors in order to fully map all nonlinearities and hysteresis caused by multiple loads. The trade-off was considered appropriate because the calibration techniques were being developed and full documentation of worst-case errors was desired. The most significant errors were saturation and hysteresis, not pure random errors, as evidenced by figure 5.

TABLE 3.– CALIBRATION REGRESSION SUMMARY: ROTOR LOAD-CELL SYSTEM rms ERRORS

| Axis | Single loads[a] | Single loads[b] | Double loads[b,c] | Triple loads[b,c] | Double-plus-triple loads[b,c] | Design prediction |
|---|---|---|---|---|---|---|
| $X$, lb | 209 | 46 | 135 | 295 | 218 | 21 |
| $Y$, lb | 87 | 41 | 67 | 30 | 105 | 89 |
| $Z$, lb | 68 | 62 | 94 | 58 | 98 | 126 |
| $L$, ft-lb | 392 | 380 | 583 | 134 | 684 | 266 |
| $M$, ft-lb | 347 | 258 | 522 | 193 | 578 | 238 |
| $N$, ft-lb | 426 | 92 | 291 | 383 | 409 | 153 |

[a] Hysteresis errors included.
[b] Hysteresis errors removed.
[c] Reduced range (±50%).

## Calibration Matrix Selection

If the RSRA load-measurement system were perfectly linear and consistent, then any sufficiently large data set would have yielded an acceptable calibration matrix valid over the entire flight envelope. However, these conditions of linearity and consistency were not met, as is evident from table 3; a thorough evaluation of possible calibration matrices against different accuracy criteria was, therefore, necessary.

This problem was partially addressed during the calibration by trying to match expected flight loads with the triple-loads data set. However, the wide disparity of errors shown in table 3 for different data sets aroused suspicion that such an a priori judgment of appropriateness might not be adequate. Fortunately, the availability of independent torque measurements using strain gages on the rotor shaft allowed candidate matrices to be tested for actual in-flight performance in the important torque ($N$) axis. A good matrix should show only small differences in torque-load measurement compared with the rotor-shaft strain-gage outputs.

Another consideration in selecting a calibration matrix is the choice of reference data set for comparing accuracy. If the regression is done correctly, the derived matrix will automatically match its parent data set better than any other possible matrix. For consistent comparisons, a standard data set representing in-flight loads should be used for evaluating the load-prediction errors of each matrix. This is logically the triple-loads data set, even though the triple-loads matrix itself may be eliminated for failing to meet other accuracy criteria. Also, any candidate calibration matrix should give small load-prediction errors based on its parent data set. Otherwise, the statistical reliability of its deriving regression would be doubtful.

There are thus three criteria for choosing a calibration matrix: (1) for a good match to actual flight conditions, it should closely match the rotor-shaft strain-gage measurements of torque ($N$); (2) for consistency, it should give low load-prediction errors for the triple-loads data set; and (3) for statistical reliability, it should give low errors for its parent data set.

A variety of matrices derived from different combinations of the basic data sets were evaluated against all three criteria. Appendix D includes a sample of the results. The preferred matrix was chosen by first eliminating all candidate matrices that failed to match the rotor-shaft strain-gage torque measurements to within 1% of full-scale torque. Data from two flights were used: a large number of data points for a variety of hover and low-speed maneuvers, and a limited number of data points for carefully stabilized hovers. Because rotor lift ($Z$) is the most critical research parameter for accuracy, the next step was to eliminate matrices with relatively high lift-measurement errors (greater than 200 lb). Inspection of the few remaining matrices showed that those derived from the double-plus-triple-loads data set best met the selection criteria.

This choice was double-checked by constructing a simple numerical accuracy index. Each matrix was applied to both the reference triple-loads data set and the matrix's parent data set to determine rms prediction errors. Errors in each axis were normalized with respect to the full-scale load in that axis. Each matrix was also applied to the flight data to determine the normalized rms errors in torque relative to rotor-shaft strain-gage measurements. All normalized rms errors were added together for each matrix to form the error indices. Again, the double-plus-triple-loads matrix was favored for having the lowest sum.

In both evaluations, the matrix derived using an indirect regression gave slightly better results than that derived using a conventional regression analysis. Table 4 shows the rms load-prediction errors for the preferred matrix when applied to the triple-loads data set.

TABLE 4.– TOTAL MEASUREMENT ROOT-MEAN-SQUARE ERRORS, BASED ON THE DOUBLE-PLUS-TRIPLE-LOADS MATRIX (HYSTERESIS ERRORS REMOVED)

| Axis | Calibration facility accuracy | Triple-loads predictions | Inertial effects | Aircraft data system | Total | Full-scale loads |
|---|---|---|---|---|---|---|
| $X$, lb | 17 | 323 | 17 | 8 | 324 | ±8,620 |
| $Y$, lb | 7 | 103 | 10 | 23 | 106 | ±5,420 |
| $Z$, lb | 37 | 169 | 2 | 28 | 175 | -48,800 |
| $L$, ft-lb | 32 | 303 | 15 | 108 | 324 | ±16,650 |
| $M$, ft-lb | 70 | 336 | 26 | 63 | 350 | +25,000<br>-16,650 |
| $N$, ft-lb | 93 | 407 | 10 | 35 | 419 | +58,200 |

## CORRECTIONS FOR KNOWN ERROR SOURCES

There are two major potential sources of error not accounted for by the regression analysis: inertial effects owing to maneuvers, and aircraft data-system errors. The first can be adequately corrected by physical analysis, and the second can be minimized by a separate calibration.

### Inertial Effects

As the RSRA maneuvers, the accelerations it undergoes act on the mass of the transmission and rotor system to produce inertial forces. These add to the measured forces, requiring corrections in the derivation of rotor forces. Fortunately, these inertial effects are calculable, hence correctable, as discussed by Condon (ref. 8).

Figure 9 illustrates the problem. The total force measured by the load cells, $\vec{F}_L$, is the sum of the aerodynamic rotor force $\vec{F}_R$ and the inertial force $\vec{F}_{IT}$ acting at the combined center of gravity of the rotor, transmission, and main engines. To get the true aerodynamic rotor force $\vec{F}_R$, $\vec{F}_{IT}$ must be calculated, transformed into $\vec{F}_{IR}$ (in rotor-head axes), and subtracted from $\vec{F}_L$. In equation (1), $\vec{F}_L$ is approximated by $\vec{CL}$, and $\vec{F}_{IR}$ is equivalent to $M_R\vec{A}_R$. The full set of equations for the inertial forces $\vec{F}_{IR}$ is developed in appendix B. For the special cases of stable hover and level flight, in which pitch, roll, and yaw rates and accelerations are all negligible, the corrections can be greatly simplified. The reduced set of equations, discussed below, was used for analysis of hover data covered by this paper.

Inertial forces $X_{IT}$,$Y_{IT}$, and $Z_{IT}$ are equal to the transmission mass times gravity, corrected for the aircraft attitude. The engines are mounted on universal joints in such a way that their effective mass, as felt by the transmission, is different in the $X$-, $Y$-, and $Z$-directions. As a result, the total effective transmission mass, including the engine and rotor masses, is different in each direction. The resulting equations can be written as follows for inertial forces at the transmission center of gravity:

$$X_{IT} = -m_{TX}\, g \sin\theta \tag{5}$$

$$Y_{IT} = +m_{TY}\, g \sin\phi \tag{6}$$

$$Z_{IT} = +m_{TZ}\, g \cos\theta \cos\phi \tag{7}$$

where $m_{TX}$, $m_{TY}$, and $m_{TZ}$ are the total effective transmission masses in each direction, $g$ is the gravity constant, and $\theta$ and $\phi$ are pitch and roll attitudes, respectively. The $IT$ subscripts refer to an inertial reference axis system at the transmission center of gravity.

There are also moments resulting from inertial effects and applied torques. In hover, the most important are rolling moments caused by total main-engine input torque and tail-rotor drive-shaft reaction torque. Neither the main-engine input shafts nor the tail-rotor drive shaft are exactly perpendicular to the main-rotor shaft, so there are also small effects on main-rotor torque. The inertial moment equations are

$$L_{IT} = QE \sin\alpha - QT \sin\beta \tag{8}$$

$$M_{IT} = -(m_{TX} - m_{TZ})d_1\, g \sin\theta \tag{9}$$

$$N_{IT} = -QE \cos\alpha + QT \cos\beta \tag{10}$$

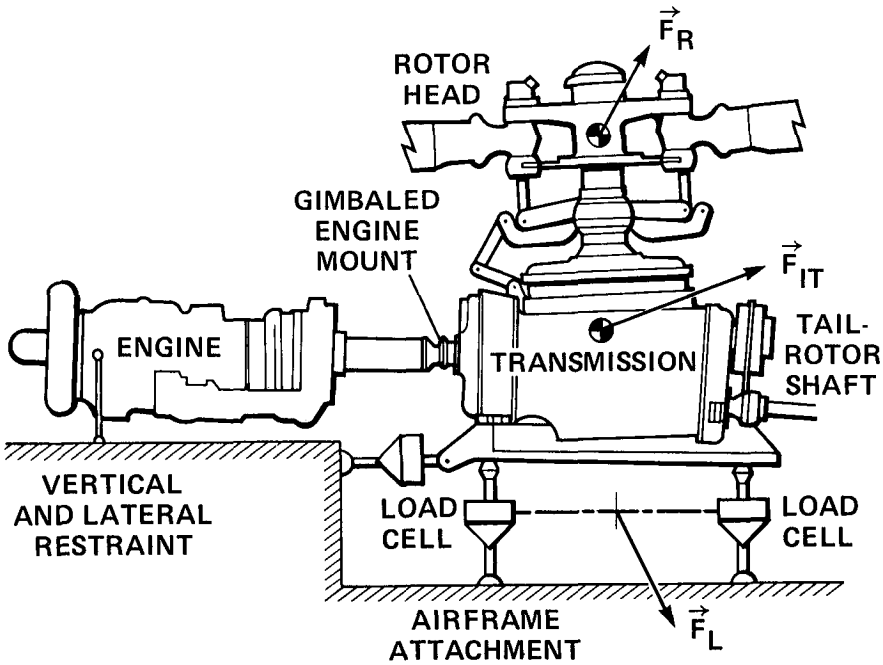


Figure 9.– Side view of the rotor force- and moment-measurement system and rotor-drive system.

where $QE$ is the total main-engine torque, $QT$ is the tail-rotor drive-shaft reaction torque, and $\alpha$ and $\beta$ are the intersection angles of the transmission output shaft with the main-engine input shafts and tail-rotor drive shaft, respectively. Engine-shaft torque is largely canceled by engine-case reaction torque; the $QE$ terms may consequently be neglected. Additional engine mass felt in the longitudinal direction ($m_{TX} - m_{TZ}$) causes a small pitching moment $M_{IT}$. The moment arm $d_1$ is the vertical distance from the transmission center of gravity to the aft engine mount.

Note that equations (5)–(10) have been revised compared with the equivalent equations (4)–(9) in Acree (ref. 3). This is so that they may be compared more directly with those derived in appendix B. These inertial forces and moments must be transferred from the inertial-reference axis system to the rotor-head axis system to allow proper correction of calibrated load measurements. This is done by using a geometric transformation matrix derived directly from the transmission design dimensions (see appendix B).

Inertial-effects calculations and axis-system transformations are straightforward and reliable enough that no overall calibration is necessary, largely because the transmission is extremely rigid and is manufactured to very close tolerances. However, there are errors in the original measurements of $\theta$, $\phi$, $QE$, and $QT$. Pitch and roll attitudes $\theta$ and $\phi$ are measured by attitude gyros, engine torque $QE$ by hydraulic torque sensors, and tail-rotor torque $QT$ by strain gages on the tail-rotor drive shaft. All such sensors were individually calibrated. Their calibration errors were converted by equations (5)–(10) to inertial forces and moments and then transferred to the rotor-head axis system to get the equivalent rotor-load rms errors shown below. (Substitution of more reliable sensors with updated individual calibrations resulted in lower errors than reported in ref. 3.)

| $X$ | $Y$ | $Z$ | $L$ | $M$ | $N$ |
|---|---|---|---|---|---|
| 17 lb | 10 lb | 2 lb | 15 ft-lb | 26 ft-lb | 10 ft-lb |

## Aircraft Data System

Figure 10 is a flowchart of flight-data recording and processing for the load-cell data channels. The load-cell data system has been upgraded to include PCM recording, but only the FM system shown here was used for the 1981 hover flight tests; consequently, it alone will be discussed. For the load-cell data outputs, each data point is an average of 10 sec of raw data. To calibrate each channel, a known test signal replaced each load cell in turn, and was processed exactly as flight data except for final calibration corrections. Sample results for one channel are shown in figure 11.

Calibration results for almost all load-cell channels were nonlinear, probably because of the VCOs (voltage-controlled oscillators) in the aircraft FM data recording electronics. The VCOs have excellent specified accuracies (less than 0.25% of full-scale), but this is misleading because nominal VCO full-scale range is greater than required to match maximum load-cell outputs during calibration. Fortunately, the load cells are rarely used over their full load range in flight, and never so in hover; the data-system calibration corrections were accordingly optimized for the load range of interest (usually all positive or all negative loads). The dashed line in figure 11 represents such an optimized calibration line. Resulting rms errors, transferred to the rotor-head axes using the double-plus-triple-loads matrix, are given below:

| $X$ | $Y$ | $Z$ | $L$ | $M$ | $N$ |
|---|---|---|---|---|---|
| 8 lb | 23 lb | 28 lb | 108 ft-lb | 63 ft-lb | 35 ft-lb |

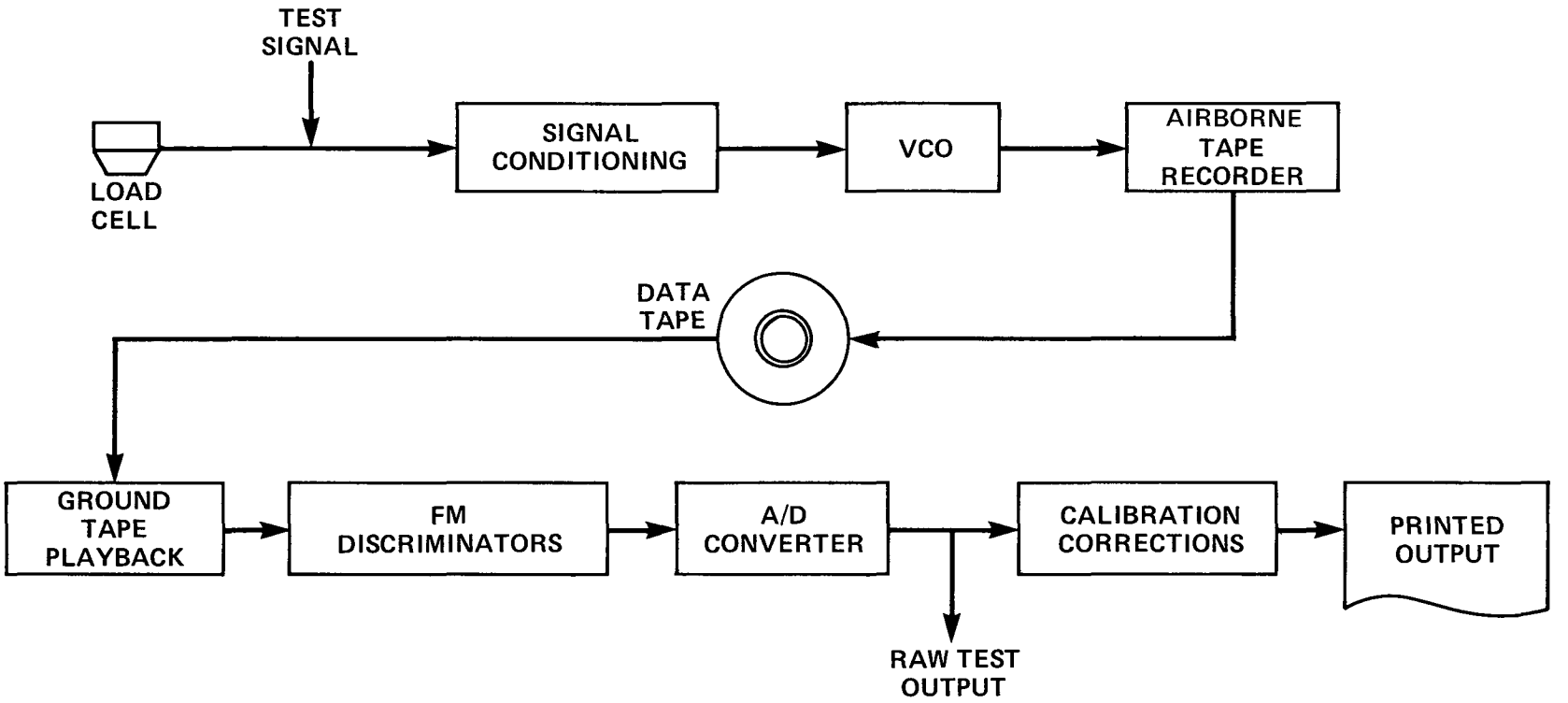


Figure 10.– Flowchart of load-cell flight data processing.

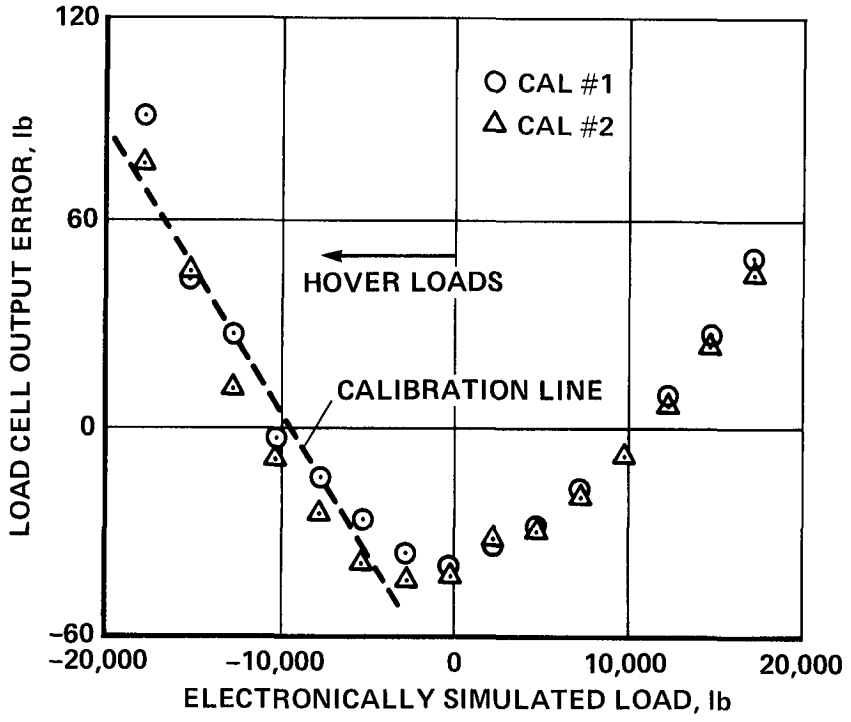


Figure 11.– Forward torque load-cell data system calibration results.

## SUMMARY OF MEASUREMENT ERRORS

RSRA rotor-load-measurement system errors resulting from all sources are summarized in table 4, using the double-plus-triple-loads correction matrix applied to triple-loads data and assuming that hysteresis errors are negligible in flight. The rms error sum is given in the Total column; design full-scale loads are also given for comparison. The results are more conservative and more reliable than those in Acree (ref. 3).

In two cases shown in table 4, $Z$ and $N$, the total errors are less than 1% of the design full-scale loads, and for $Y$, $L$, and $M$ they are less than 2%. This is excellent performance for such a wide load range. With over 3.8% error, $X$ remains relatively poor.

These are by no means the limits of RSRA rotor-load-measurement accuracy. Better load-cell rod-ends for lowered hysteresis, an improved aircraft-data system, and closer simulation of flight conditions during static calibration could all potentially improve calibrated accuracy. The calibration matrix also may be more closely optimized for a particular measurement. All such measures will be explored as research requirements dictate.

## FLIGHT-TEST VALIDATION

A series of flight tests was conducted in 1981 to verify (among other research objectives) performance of the calibrated rotor-load-measurement system in flight. Checking the amount of measurement hysteresis and tracking gross weight changes caused by fuel burnoff were the major test activities pertaining specifically to the load-measurement system. Measurement of fuselage vertical drag in hover was a closely related research task; it is reported in full by Flemming and Erickson (ref. 1). These flights also provided the reference data used for choosing the optimum calibration matrix.

### Hysteresis Checks

A key assumption used in the analysis of calibration data is that static hysteresis is eliminated in flight by the dithering effect of vibratory rotor loads. This assumption was tested in hovering flight by accelerating the aircraft as smoothly as possible through pure longitudinal, lateral, and vertical translations, then smoothly returning to a hover. Each such maneuver was performed several times in both the positive and negative directions.

By comparing hover rotor-load measurements taken after approaching hover from different maneuvers in opposite directions, the amount of hysteresis actually present in flight was determined. The comparisons were complicated by trim errors; that is, errors owing to the impossibility of perfectly duplicating a given hover condition under actual flight conditions. No hysteresis larger than the scatter resulting from trim errors and measurement random errors was detected by such comparisons.

Main-rotor torque measurements were a special case worth discussing in some detail. For these flights, there were redundant torque measurements, using strain gages mounted on the rotor shaft. Although not perfect measurements of torque, the strain-gage data were at least subject to different error mechanisms than the load-cell data, so that there were no common hysteresis errors that could have canceled each other. Calibrations of the strain gages have yielded errors of less than 1% of full-scale torque. No torque hysteresis was detectable when comparing load-cell and strain-gage outputs from the flight-data processing shown in figure 10.

Load-cell measurements of torque are plotted in figure 12 against strain-gage data for stable hovers approached by increasing or decreasing torque. To avoid confusing the hysteresis check with the regression analysis, no calibration corrections were included; thus, there is a slight slope error, but any hysteresis errors are better revealed.

A slight amount of residual hysteresis between the increasing and decreasing torque cases is detectable in figure 12. Regression analysis showed a hysteresis band 386 ft-lb wide that was significant at the 95% level. However, at the same confidence level, the reference strain-gage error was 408 ft-lb; and the measurement system rms error for $N$ in table 4, without hysteresis, is 419 ft-lb, for an approximate 838 ft-lb error at the 95% level. These statistics are not rigorously comparable; nevertheless, they indicate that hysteresis can be neglected for present research purposes.

### Lift Measurement in Hover

As the RSRA hovers, the burnoff of fuel lowers its gross weight. Fuel consumption can be measured with fuel totalizers, so by plotting measured lift against known gross weight, a good check of load-measurement-system performance can be made. Figure 13 shows the results for out-of-ground-effect (OGE) hover. Each plotted point represents an average of 10 sec of raw data. Scatter caused by trim errors is considerable, but measured lift can be seen to track true gross weight very well. If fuselage net vertical drag were zero, measured lift would exactly equal true gross weight; this determines the zero vertical drag line of the plot. The vertical offset from this line is the amount of vertical drag; it should be nearly constant for a given altitude and identical flight conditions. Figure 13 shows that it is indeed almost constant during OGE hover for different gross weights, leading to the conclusion that the rotor-load-measurement system performs as designed.

## OTHER CALIBRATIONS

Calibration of the rotor-load-measurement system was the most important of several calibrations performed on the RSRA. Load-measurement systems for the tail rotor, wing, and auxiliary engines (fig. 1) were also calibrated at the same time as the rotor-load-measurement system. The helicopter version of the RSRA has a differently configured rotor-load-measurement system (refs. 2 and 5), which has also been calibrated. These additional calibrations are discussed very briefly below.

### Tail Rotor

The RSRA has a simple system for measuring tail-rotor thrust (fig. 14), with a single load cell mounted diagonally across a parallelogram support for the tail-rotor gearbox. Its calibrated load range is +3,250 lb to the right (thrusting into the tail pylon) to −1,000 lb to the left, although its maximum potential load range is slightly higher. Calibration reference accuracy is less than 3 lb (less than 0.1% full scale), and best-possible system accuracy is 7 lb (0.2% full scale).

The major error mechanism was hysteresis, caused by the load-cell rod-end bearings and the bearings at the corners of the parallelogram support. There was also a very small amount of sliding friction caused by a spring-loaded safety pawl, which is designed to lock the parallelogram in position if the load cell should fail.

A conventional two-variable regression was used to analyze the data. To eliminate the hystereses effects from the analysis, increasing-load and decreasing-load data were analyzed separately and the results averaged.

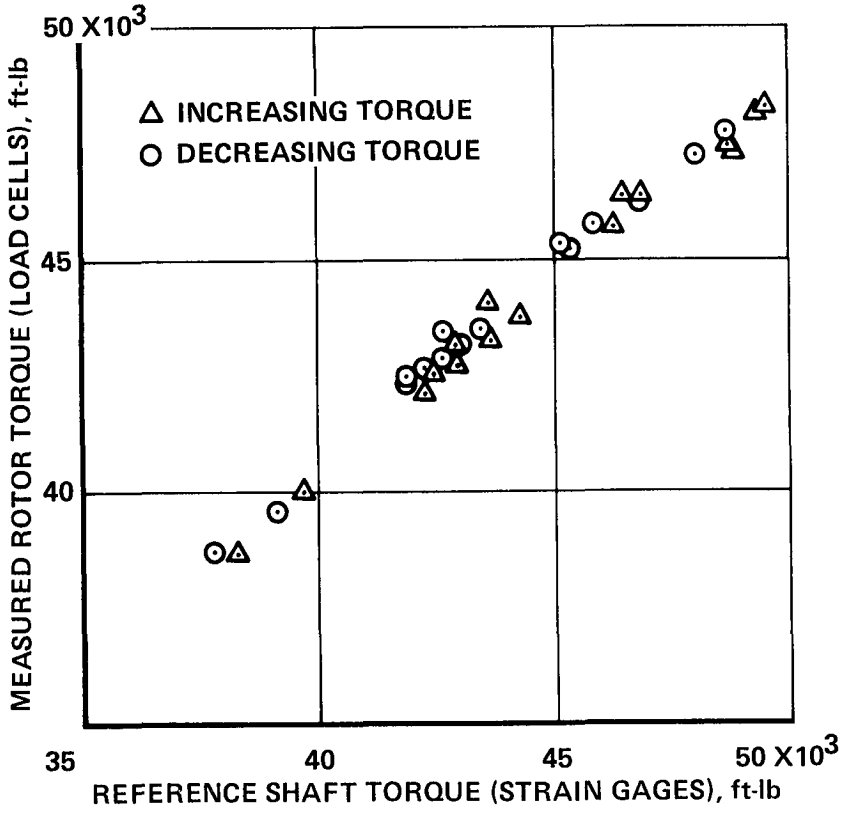


Figure 12.– Comparison of rotor torque measurements by load cells and strain gages during hover.

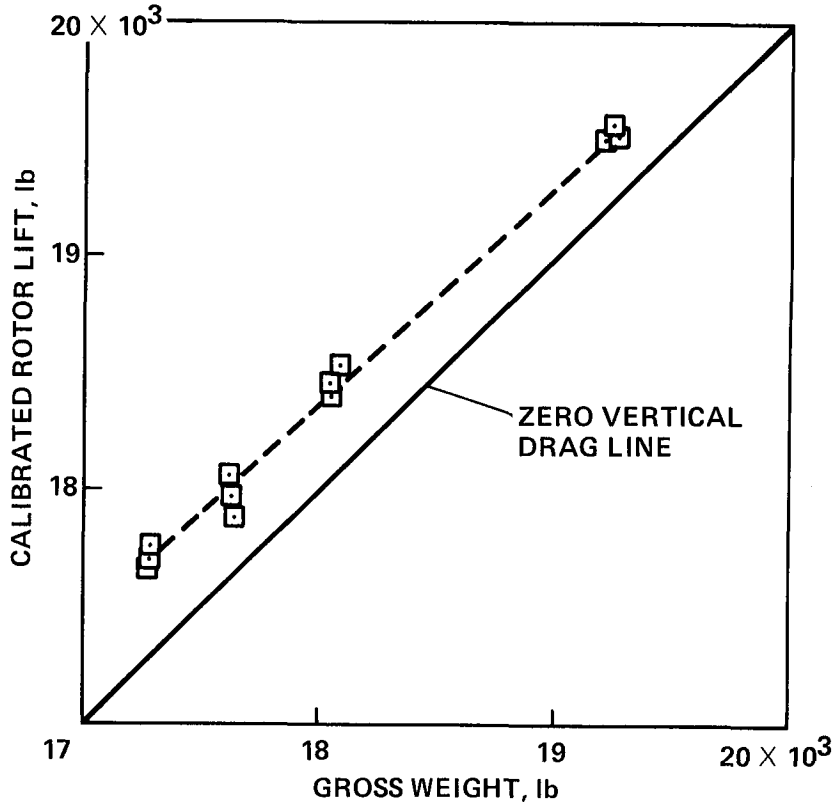


Figure 13.– Load-cell system lift measurement versus corrected gross weight for OGE hover.

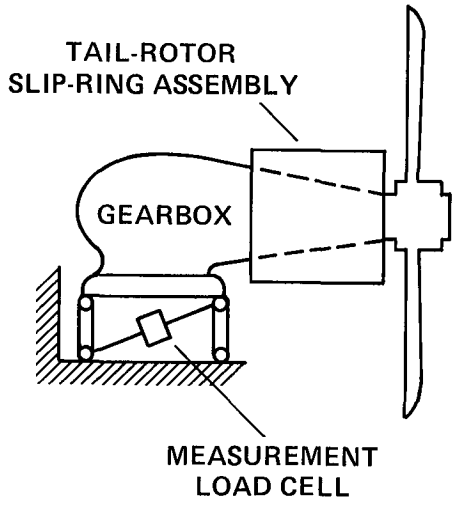


Figure 14.– Tail-rotor thrust measurement system.

Averaged regression error was 42 lb, and aircraft data system error was 4.4 lb. Including calibration errors, this gives a total rms error of 43 lb (1.3% full scale). Tail-rotor vibrations should effectively eliminate the hysteresis, allowing this accuracy to be achieved in flight.

There is a small inertial load owing to the mass of the tail-rotor gearbox, discussed in appendix B.

### Wing and Auxiliary Engines

The compound version of the RSRA has a wing-load-measurement system (ref. 8), which was calibrated at the same time as the rotor system. Preliminary analysis of its calibration data revealed mechanical interference similar to the redundant-link interference (fig. 5), but much more severe. Consequently, modification and recalibration of the system is required before research-quality results can be obtained. Completion of this work is now scheduled for mid-1984.

The auxiliary thrust engines on the compound RSRA have simple thrust-measurement systems. Calibration revealed excessive hysteresis and other nonlinearities. Extensive modification of the auxiliary engine load-cell systems is required to achieve useful performance.

### RSRA Helicopter

A second calibration was performed on the pure-helicopter version of the RSRA, which has a completely different rotor-load-measurement system. The vertical load cells are in a focused configuration, and for longitudinal, lateral, and torque measurements there are active isolators (refs. 2 and 5). These units are designed primarily to isolate the airframe from rotor vibrations in the horizontal plane, but also have hydraulic load sensors to take the place of load cells. The second RSRA was calibrated in essentially the same way as the first, but final results are not expected to be at all similar. A compilation of important data from this calibration is available in Acree (ref. 5).

## FUTURE REFINEMENTS

Two broad categories of refinements to the rotor-load-measurement system and its calibration are possible: improvements to the aircraft itself, and changes in the calibration facility and procedures. Some of the facility improvements were implemented for the calibration of the second RSRA (refs. 4 and 5).

### Improved Aircraft Systems

Elimination of data saturation caused by premature redundant-link lock-up is an obvious improvement. The required mechanical changes to the aircraft are simple, but will require extensive study for safety-of-flight assurance before they are implemented.

Preliminary experiments on isolated load-cell rod-ends indicate that rod-end bearing friction is the dominant source of hysteresis; therefore, replacing the existing rod-ends with better units, such as elastomeric bearings, could greatly reduce hysteresis. This may also help the overall quality of the calibration by improving repeatability and eliminating suspected nonlinear hysteresis effects.

Changing the load-cell flight-data recording and processing from FM to PCM has been completed; it promises definite improvements in performance.

### Improved Calibration Method

Progressive improvements to the calibration facility to achieve more realistic simulation of flight conditions are being implemented. New data and load-control systems allow more multiple-load data to be collected, and it is also possible to apply some multiple loads beyond the original limits of ±50% of full-scale design load (ref. 4). These refinements allow a greater variety of calibration data sets to be applied, which should help in finding a more accurate calibration matrix which is better matched to actual flight conditions.

An automated calibration-data scanning and recording system allows much more data, including replications, to be taken during load application. This should result in better definition of hysteresis, zero-crossing errors, and skewed data. A slight reduction of calibration reference errors, mostly because of decreased electronic drift errors, is also possible. The automated system indirectly allows better data management, hence more efficient regression analysis.

More extensive aircraft-alignment instrumentation has also been installed along with the new data system. Together, the combination provides continuous recording of all alignment data, thereby allowing automatic correction of applied-load data to correct for the effects of imperfect aircraft alignment in the facility. This also provides the option of opening up the 0.5° alignment tolerance, thus simplifying calibration procedures.

Better hydraulic load-control hardware provides much smoother load application and considerably eases the task of precisely controlling loads. The data in reference 5 indicate that this eliminates such problems as zero-crossing errors and skewed data, which are believed to have resulted from imperfect load application.

Addition of a dither, or vibratory loads, to simulate rotor vibrations is also highly desirable. Such improvements would, however, require considerable modification of the calibration facility and would have to be carefully studied because of their potential effect on the airworthiness of the aircraft. Addition of a multiple-load dither would result in a "quasi-static" calibration. A true full-scale dynamic calibration, although highly desirable, would be a completely different undertaking and lies somewhat further in the future.

## CONCLUSIONS

The first-full-system static calibration and analysis of the compound RSRA rotor-load-measurement system have been completed. Optimizing the data analysis for the case of stable hover yielded good results for total system accuracy: less than 2% of full-scale load for most axes. Hysteresis was identified as a potential source of calibration error, but flight tests confirmed the hypothesis that hysteresis was negligible under actual flight conditions. Further flight tests showed that the load-measurement system performed accurately enough to allow direct measurement of fuselage vertical drag in hover.

Ames Research Center
National Aeronautics and Space Administration
Moffett Field, California 94035, January 24, 1984

# APPENDIX A

## ESTIMATES OF LOAD-MEASUREMENT-SYSTEM ERRORS

### ERROR PROPAGATION

In order to make usable comparisons between different errors, and between errors and full-scale loads, all errors must be expressed as equivalent loads in a common axis system. Except where explicitly noted, all errors and loads in this appendix are in an axis system centered at the rotor head (fig. 3). The vertical axis lies along the center of the main-rotor shaft, positive down. The other two perpendicular axes lie in the plane of the flapping hinges, positive forward and right for the longitudinal and lateral directions, respectively.

Errors are not usually calculated directly in terms of this axis system. For instance, individual load-cell laboratory calibration errors are known only along the sensitive axis of each load cell. Such errors must be translated into equivalent rotor-load errors. The basic principles are given by Crow et al. (ref. 9); the method is briefly explained in terms of matrix calculations below.

The error-propagation equation can be written analogously to equation (1):

$$\vec{F}_E = C_E \vec{L}_E \tag{A1}$$

The elements of the load-cell vector $\vec{L}_E$ and the rotor-load vector $\vec{F}_E$ are variances, and the elements of the error-propagation matrix $C_E$ are the squares of the corresponding elements of the calibration matrix $C$. In the case of instrumentation calibrations – which include load cells and data system channels – mean errors can be reduced to zero by proper data processing, so that the error variances are the same as the mean sums-of-squares. Errors are always given in this paper as the square roots of the mean sums-of-squares. Since it is not generally possible to achieve zero mean errors for all axes under all applied load combinations with a given $C$-matrix, the rms regression errors are not necessarily equal to the standard deviations (regression standard errors). Therefore, rms errors must consistently be used instead of standard deviations for all summations and comparisons of errors.

Inertial-effects errors are propagated by first calculating errors caused by individual sensors in an axis system at the center of gravity of the combined engine, transmission, and rotor head. These errors are then transferred to the rotor-head-axis system by a transformation matrix derived from transmission design geometry (given in appendix B).

### ERROR PREDICTIONS

During the design and development of the RSRA, several different predictions were made of the accuracy of the rotor-load-measurement system; the most important are summarized in table A1. All of the predictions used $C$-matrices or analytically equivalent equations derived directly from the design geometry of the measurement system.

Tcheng[1] gives several different error predictions for different sets of assumptions; the two most extreme are given in table A1. Tcheng's best case assumes no errors other than individual load-cell design specification errors. His worst case includes, in addition, expected data-system and calibration errors, plus expected uncorrected interactions. Two sets of expected total errors are quoted from Corro (ref. 10) and Monteleone (ref. 11). These include inertial-effects errors, and use different assumptions of instrumentation and other errors. Two further sets of predicted errors were calculated by this author, assuming no errors other than those contributed by individual load cells, as determined by laboratory calibrations (performed in 1980). The larger errors include calibration reference load-cell errors.

Table A1 does not exhaust all available predictions of RSRA rotor-load-measurement system performance; it merely samples the wide variety of expectations of different researchers using different assumptions. It is not always possible to determine what assumptions were made and which types of error were included in any given report. Furthermore, some researchers (e.g., Condon, ref. 8) published results before all design changes were completed for the RSRA measurement system; their predictions are, therefore, invalid. The disagreement of the performance predictions given in table A1 underscore the need to conduct a full-system calibration traceable to the National Bureau of Standards.

Similar differences can be found in published calculations of total system-calibration accuracy. Tcheng gives results for an early, partial calibration. Differently optimized calibration algorithms give different accuracies for the same data. Burks (ref. 2) and Flemming and Erickson (ref. 1) give accuracies for the single-loads data regressions, but using a different and more restrictive hysteresis removal algorithm than used here; neither of these two papers includes inertial effects or data-system errors in their tables of calibration accuracies. Revised methods of matching calibration matrices to flight data also result in different accuracies (compare table 4 to the equivalent table 4 in Acree, ref. 3).

TABLE A1.– COMPARISON OF LOAD-MEASUREMENT-SYSTEM ACCURACY PREDICTIONS

| Axis | Load-cell specification errors only[a] | Worst-case analysis[a] | Design expectation[b] | Aircraft load-cell laboratory calibration errors only[c] | All load-cell calibration errors[c] | Design expectation[d] |
|---|---|---|---|---|---|---|
| $X$, lb | 21 | 96 | 141 | 4 | 17 | 96 |
| $Y$, lb | 89 | 100 | 293 | 36 | 36 | 235 |
| $Z$, lb | 126 | 320 | 344 | 52 | 64 | 335 |
| $L$, ft-lb | 266 | 798 | 631 | 195 | 198 | 1345 |
| $M$, ft-lb | 238 | 558 | 330 | 90 | 114 | 693 |
| $N$, ft-lb | 153 | 405 | 241 | 62 | 111 | 407 |

[a]Tcheng. [b]Reference 11. [c]Author's calculations based on component calibrations.
[d]Reference 10.

[1]Tcheng, P.: "The Onboard Force Measuring System of the Rotor Systems Research Aircraft (RSRA)." Unpublished paper presented at the 24th International Instrumentation Symposium, May 1978.

## APPENDIX B

## INERTIAL-EFFECTS CALCULATIONS

Linear and rotational accelerations act on the mass of the main-rotor transmission to produce inertial forces and moments. Although not produced by the rotor, these inertial effects are seen by the load cells and are indistinguishable from rotor aerodynamic loads. The resulting measurement errors can be calculated and removed from the data. Similar errors also arise from gyroscopic precession of the rotating components of the two engines and the main-rotor transmission. The analysis presented here is an extension of that reported by Condon (ref. 8).

Figure B1 shows the layout of the engines and transmission, with important dimensions labeled. The main-rotor shaft is inclined 2° forward of the vertical aircraft body axis (fig. 3 in the main body of this paper). The engines are tilted 2° nose-up from the airframe horizontal, so that there is a total angle of 86° between the engine shafts and the main-rotor shaft. The tail-rotor drive shaft is inclined 6.13° below the horizontal. The main-rotor hub and rotating swashplate are included in the transmission mass, but not the flapping mass of the rotor blades.

## EFFECTIVE MASSES

The analysis is complicated by the nonrigid mounting of the engines. The forward mounts restrain the engines vertically and laterally, but not longitudinally along the engine-shaft centerline. Furthermore, the aft mount is gimbaled and attached to the transmission. The transmission consequently reacts to all longitudinal engine forces, but only a fraction of vertical or lateral forces. The effective combined inertia (mass) of the transmission and engines is thus greater in the $X$-direction than in the $Y$- or $Z$-directions.

The most convenient way of handling such differences in effective engine-mass contributions is to separate the engine mass into two components: that fraction contributing to vertical and lateral forces, and the larger component contributing to longitudinal forces. Transmission mass $m'_T$, center of gravity, and moments of inertia $I'_{TX}$, $I'_{TY}$, and $I'_{TZ}$ are calculated including only the smaller value of engine mass for all directions. The additional engine mass $m$ in the longitudinal direction is accounted for by the following equations:

$$X_{I_{\dot{u}}} = -(m'_T + \Delta m_E)\dot{u} \tag{B1a}$$

$$= -m_{TX}\dot{u} \tag{B1b}$$

$$M_{I_{\dot{u}}} = -\Delta m_E d_1 \dot{u} \tag{B2}$$

$$X_{i_{\dot{q}}} = -\Delta m_E d_1 \dot{q} \tag{B3}$$

$$M_{I_{\dot{q}}} = -(I'_{TY} + \Delta m_E d_1^2)\dot{q} \tag{B4a}$$

$$= -I_{TY}\dot{q} \tag{B4b}$$

Note that the $\Delta m_E$ contributions to $X_{I_{\dot{u}}}$ and $M_{I_{\dot{q}}}$ may be incorporated into the effective longitudinal mass $m_{TX}$ and pitching moment of inertia $I_{TY}$.

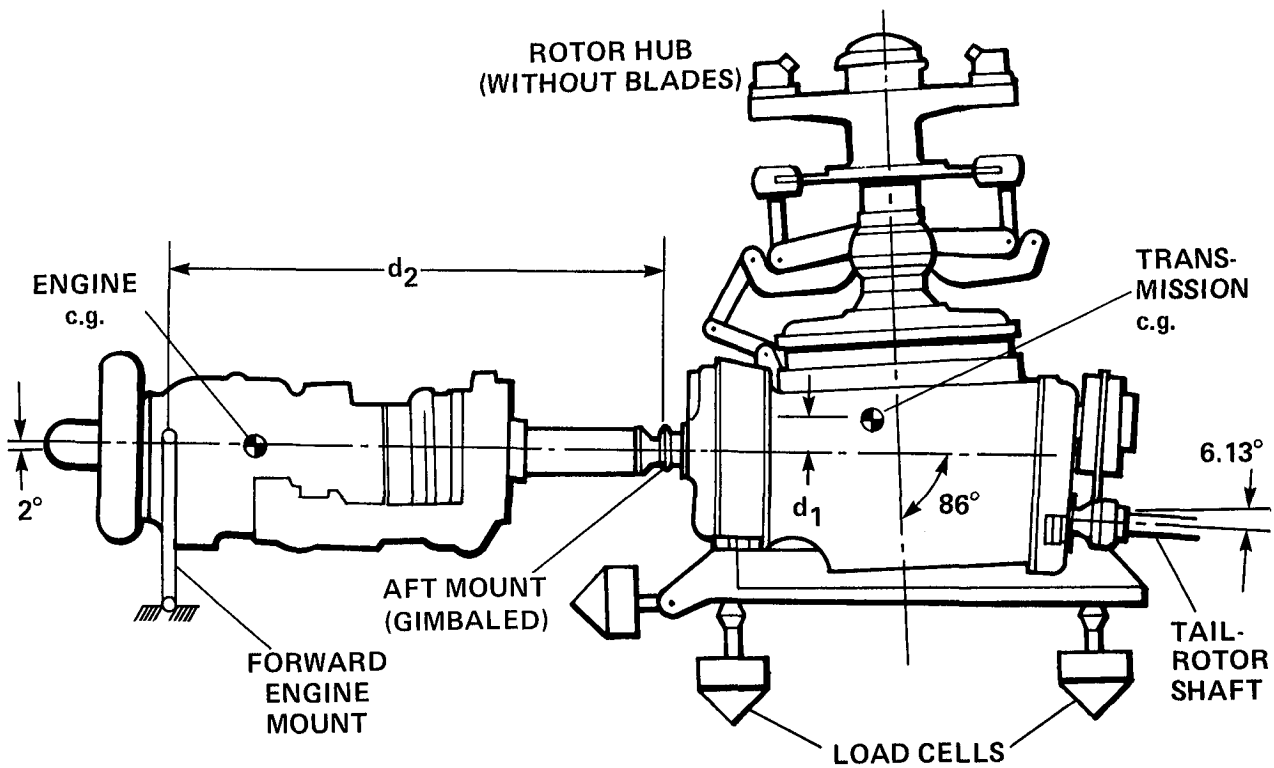


Figure B1.– Main transmission and engine components contributing to inertial effects.

The load cells themselves cause similar effects, but at lower magnitudes. The mass of each load cell between its electrical (force-sensing) center and the transmission must be considered as part of the transmission mass. Each load cell is mounted at both ends with spherical bearings acting as ball joints. The transmission therefore feels about one-half of each load cell's mass in directions perpendicular to the load cell's sensitive axis. Also, the electrical center of each load cell is offset slightly from its center of mass. The effective inertial mass of each load cell as seen by the transmission is thus different in each direction. However, the differences are sufficiently small that they may be ignored with negligible error in the case of the load cells. One-half load-cell mass was used consistently for calculating all contributions in all directions.

## INERTIAL EFFECTS OF ACCELERATIONS

If linear and rotational accelerations are measured at the transmission, the loads seen by the load cells owing to such accelerations may be expressed as inertial loads at the transmission center of gravity:

$$X_{I_A} = -m_{TX}\dot{u}_T - \Delta m_E d_1 \dot{q} \tag{B5}$$

$$Y_{I_A} = -m_{TY}\dot{v}_T \tag{B6}$$

$$Z_{I_A} = -m_{TZ}\dot{w}_T \tag{B7}$$

$$L_{I_A} = -I_{TX}\dot{p} \tag{B8}$$

$$M_{I_A} = -I_{TY}\dot{q} - \Delta m_E d_1 \dot{u}_T \tag{B9}$$

$$N_{I_A} = -I_{TZ}\dot{r} \tag{B10}$$

If it is assumed that the maximum rotational accelerations are 2 rad/sec$^2$ in roll ($\dot{p}$) and 1 rad/sec$^2$ in pitch and yaw ($\dot{q}$ and $\dot{r}$), then all moments owing to cross-products of inertia are of the order of 0.1% full-scale load or less in the relevant axis. The appropriate terms in equations (B8)–(B10) have accordingly been deleted. The roll-acceleration limit applies to the helicopter version of the RSRA; the limit would be lower for the compound or fixed-wing versions (described by Burks, ref. 2).

All accelerations must be referenced to the transmission center of gravity for the above equations to be valid. The accelerometer package cannot be mounted physically inside the transmission, so measured linear accelerations $\dot{u}_A$, $\dot{v}_A$, and $\dot{w}_A$ must be transformed to transmission accelerations $\dot{u}_T$, $\dot{v}_T$, and $\dot{w}_T$ by the following equations:

$$\dot{u}_T = \dot{u}_A - d_Z\dot{q} + d_Y\dot{r} \tag{B11}$$

$$\dot{v}_T = \dot{v}_A - d_X\dot{r} + d_Z\dot{p} \tag{B12}$$

$$\dot{w}_T = \dot{w}_A - d_Y\dot{p} + d_X\dot{q} \tag{B13}$$

There are also terms in $p^2$, $q^2$, and $r^2$, but their effects are all negligible if it is assumed that the maximum steady rotational rate in any axis is 0.26 rad/sec (15°/sec).

## INERTIAL EFFECTS OF STEADY ROTATIONS

The transmission gears have angular momenta in both the vertical and longitudinal directions, but only the vertical component is significant. Processional moments resulting from steady rotations are, thus,

$$L_{I_G} = H_G q \tag{B14}$$

$$M_{I_G} = -H_G p \tag{B15}$$

The precessional yaw moment $N_{I_G}$ is negligible (less than 0.1% full-scale yaw load), assuming the maximum rates given in the preceding section.

There are also precessional moments caused by the angular momenta of the engines. The aft engine mounts are gimbaled and cannot transmit moments perpendicular to the engine-shaft axis. Any engine precessional moment is consequently felt by the transmission as one component of a force couple. Given the previously assumed rate limits, only one such force is significant:

$$Y_{I_E} = H_E \frac{1}{d_2} \cos 2^\circ \, q \tag{B16}$$

Note that engine moment of momentum is given in the engine-shaft axis, but dimensions are given in aircraft body axes that are inclined 2° nose-down from the engine shafts (fig. B1).

All possible force couples acting at the engine mounts were analyzed to determine resulting moments on the transmission. Again, only one such force caused a significant moment:

$$L_{I_E} = -Y_{I_E} d_1 \tag{B17a}$$

$$= -H_E \frac{d_1}{d_2} \cos 2^\circ \, q \tag{B17b}$$

For most purposes, these inertial effects owing to engine precessional torques may be neglected. For the assumed pitch-rate limit, maximum $Y_{I_E}$ is less than 0.5% full-scale side force, and $L_{I_E}$ is only 0.2% full-scale roll moment.

## APPLIED TORQUE ERRORS

Although not true inertial effects, applied engine-input torques and tail-rotor drive-shaft reaction torque must be accounted for. It is convenient to lump these effects together with inertial effects before final transformation to rotor-head calibration axes.

The only significant applied moment caused by engine output torque is

$$L_{I_{QE}} = QE \cos 2^\circ \tag{B18}$$

However, most of the engine-case reaction torque is also taken up by the transmission through the aft engine mounts, largely canceling the engine shaft torque. Therefore, $L_{I_{QE}}$ may be assumed to be zero, but if roll measurements must be made to maximum possible accuracy, engine case reaction torque will have to be explicitly measured.

Measurements of tail-rotor drive-shaft torque are available, and the resulting applied moments are

$$L_{I_{QT}} = QT \cos 6.13° \tag{B19}$$

$$N_{I_{QT}} = -QT \sin 6.13° \tag{B20}$$

Maximum $N_{I_{QT}}$ is less than 0.3% for nearly all flight conditions and may be neglected.

## TRANSFORMATION MATRIX

The equations required to transform inertial loads from the transmission center of gravity to the rotor-head calibration axes may be expressed in matrix form:

$$\vec{F}_{IR} = T_T \vec{F}_{IT} \ , \quad \text{or} \tag{B21a}$$

$$\begin{bmatrix} X_{IR} \\ Y_{IR} \\ Z_{IR} \\ L_{IR} \\ M_{IR} \\ N_{IR} \end{bmatrix} = \begin{bmatrix} \cos 2° & 0 & \sin 2° & 0 & 0 & 0 \\ 0 & 1 & 0 & 0 & 0 & 0 \\ -\sin 2° & 0 & \cos 2° & 0 & 0 & 0 \\ 0 & -1.528 & 0.0400 & \cos 2° & 0 & \sin 2° \\ 1.533 & 0 & -0.0915 & 0 & 1 & 0 \\ -0.0400 & 0.1449 & 0 & -\sin 2° & 0 & \cos 2° \end{bmatrix} \times \begin{bmatrix} X_{IT} \\ Y_{IT} \\ Z_{IT} \\ L_{IT} \\ M_{IT} \\ N_{IT} \end{bmatrix} \tag{B21b}$$

This matrix assumes all forces and moments are in pounds and foot-pounds, and applies only to the load-cell configuration of the RSRA.

## SUMMARY OF TRANSMISSION CONTRIBUTIONS

Inertial loads due to all significant effects, including tail-rotor drive-shaft reaction torque, may be written out as follows:

$$X_{IT} = X_{I_A} \tag{B22a}$$

$$= -m_{TX}\dot{u}_T - \Delta m_E d_1 \dot{q} \tag{B22b}$$

$$Y_{IT} = Y_{I_A} + Y_{I_E} \tag{B23a}$$

$$= -m_{TY}\dot{v}_T + H_E \frac{1}{d_2} \cos 2° \, q \tag{B23b}$$

$$Z_{IT} = Z_{I_A} \tag{B24a}$$

$$= -m_{TZ}\dot{w}_T \tag{B24b}$$

$$L_{IT} = L_{I_A} + L_{I_G} + L_{I_{QE}} + L_{I_{QT}} \tag{B25a}$$

$$= -I_{TX}\dot{p} + H_G q - H_E \frac{d_1}{d_2} \cos 2^\circ \, q + QT \cos 6.13^\circ \tag{B25b}$$

$$M_{IT} = M_{I_A} + M_{I_G} \tag{B26a}$$

$$= -I_{TY}\dot{q} - \Delta m_E d_1 \dot{u}_T - H_G p \tag{B26b}$$

$$N_{I_T} = N_{I_A} \tag{B27a}$$

$$= -I_{TZ}\dot{r} \tag{B27b}$$

Note that equation (B24) does not include the "flapping mass" of the main-rotor blades, which is 1377.7 lb.

Transformation to rotor-head calibration axes by equation (B21) is straightforward on a computer, but is too cumbersome to be written out in full here. Equations (B21) and (B22)–(B27) may be combined in matrix form as

$$\vec{F}_{IR} = T_T M_T \vec{A}_T \tag{B28}$$

This is equivalent to the $M_R\vec{A}_R$ term in equations (1) and (4) in the main body of this paper, referenced to the transmission center of gravity.

The following parameters must be measured in real time for proper inertial-effects calculations: $\dot{u}_A$, $\dot{v}_A$, $\dot{w}_A$, $p$, $q$, $\dot{p}$, $\dot{q}$, $\dot{r}$, $QE$, and $QT$. Their measurement errors must be propagated to the rotor-head axis system to determine the total inertial-effects measurement errors. Since the instrumentation configuration of the RSRA may be changed from flight to flight, these errors must be calculated separately for each configuration. A general error summary consequently cannot be given here.

Stable hover and steady straight-and-level flight are special cases of inertial-effects calculations. In both conditions, all accelerations and rotational rates are zero, except for an effective vertical acceleration in the direction opposite to the gravity vector. Attitude measurements may be substituted for acceleration measurements in this case, and equations (5)–(10) in the main body of this paper follow directly.

## TAIL-ROTOR INERTIAL EFFECTS

The mass of the tail-rotor gearbox causes inertial loads to be felt by the tail-rotor thrust-measurement load cell (fig. 14). If the lateral acceleration of the gearbox can be measured directly, the inertial load is simply

$$T_I = -v_{TR} m_{TR} \tag{B29}$$

The general relationship between the tail-rotor gearbox and the aircraft center of gravity is shown in figure B2. The aircraft center of gravity is directly under the rotor head, and the allowable range of variation is too small to cause significant errors in moment arms $d_3$ and $d_4$.

If only aircraft body accelerations are measured, the effects of roll and yaw rotational accelerations must be taken into account. Rewriting equation (B12) for the tail rotor:

$$\dot{v}_{TR} = -\dot{v}_A - d_3\dot{r} + d_4\dot{p} \tag{B30}$$

The results may be substituted directly into equation (B29).

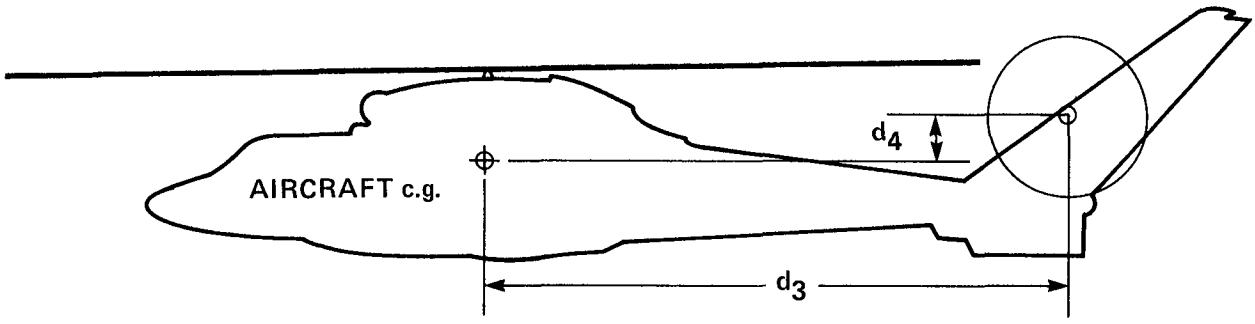


Figure B2.– Moment arms from tail rotor to aircraft center of gravity.

## APPENDIX C

## EXAMPLE OF A CALIBRATION MATRIX

The double-plus-triple-loads calibration matrix (C-matrix) is as follows:

| | | | | | | |
|---|---|---|---|---|---|---|
| -0.03814 | -0.02983 | -0.02560 | -0.01037 | -0.01796 | 0.01423 | -1.085 |
| 0.02835 | -0.05430 | -0.05958 | 0.07967 | -1.064 | 1.103 | 0.02340 |
| -0.9761 | -1.040 | -1.036 | -0.9634 | 0.02603 | -0.007958 | 0.03644 |
| 1.465 | -1.450 | 1.411 | -1.429 | 4.784 | -4.874 | 0.06048 |
| 1.650 | 1.469 | -2.111 | -1.853 | 0.1232 | -0.01741 | -5.266 |
| 0.1472 | -0.1374 | -0.3148 | 0.4101 | -1.590 | -1.749 | 0.02687 |

For load-cell data in pounds, this matrix gives forces $X$, $Y$, and $Z$ in pounds and moments $L$, $M$, and $N$ in foot-pounds.

The associated regression intercept vector $\vec{B}$ is

$X = 83.69$ lb

$Y = -13.51$ lb

$Z = -3152$ lb

$L = -512.9$ ft-lb

$M = -189.3$ ft-lb

$N = 308.1$ ft-lb

The order in which load-cell data are required in the $\vec{L}$-vector by the matrix given above is (fig. 2)

left forward vertical

right forward vertical

left aft vertical

right aft vertical

forward torque

aft torque

drag

The calibration tare vector $\vec{D}$ is

$X = 0$ lb

$Y = 0$ lb

$Z = 3640$ lb

$L = 60$ ft-lb

$M = -218$ ft-lb

$N = 6$ ft-lb

# APPENDIX D

## EXPANDED SUMMARY OF REGRESSION RESULTS

All major data sets were run with all derived calibration matrices to get errors shown in table D1. Matrices were derived from the single-, double-, and triple-loads data sets and three combinations, in all cases using an inverse-regression technique. No single-plus-triple-loads matrix was derived, because it would have used a contradictory combination of the least and most realistic data, and therefore would reveal no useful insights into system behavior. Also used was a geometric matrix derived directly from system design dimensions assuming total rigidity and perfect construction.

Applied-load errors are given for the same axis as the applied, or varied, load in table D1. For double loads, the errors were averaged over all combinations of varied loads in the error axis and constant loads in other axes. Table D2 similarly gives errors averaged over all applied loads for each measurement axis. Linear hysteresis errors are not included in either case.

In general, the lowest errors for a given data set are produced by a matrix derived from that data set. There are occasional exceptions for individual axes, but this generalization holds true if errors in all six axes are considered together. Average errors (table D2) are usually lower than corresponding applied-load errors, but there are numerous exceptions. The exceptions arise when an applied load is significantly greater than the full-scale load in an interacting measurement axis; the effects of any slope errors or nonlinearities are thereby exaggerated.

Although the geometric matrix has reasonably low errors for the single-loads data set, it is far from the best matrix for the multiple-loads data sets. This is an example of interaction errors: a load in one axis can change the response of another axis. The direct physical cause is thought to be unequal load sharing among the vertical load cells because of manufacturing and rigging tolerance error accumulations. This clearly shows the need for full calibration of the system and complete regression analysis.

Also of interest is the poor performance of the triple-loads matrix for the single- and double-loads data sets; note especially the double-loads moment ($L$, $M$, and $N$) errors. This indicates that the triple-loads matrix was overoptimized for its parent data set. By contrast, the double-plus-triple-loads matrix gives acceptable errors for both the double-loads and triple-loads data sets. This relative insensitivity to exact loading conditions is the reason this matrix was chosen for flight data reduction.

The inferior performance of the triple-loads matrix admittedly throws into question the validity of using the triple-loads data set as the basic error reference (table 4). Unfortunately, there is no better reference data set available. The double-plus-triple-loads data set may produce a better calibration matrix for general use (see the section entitled Calibration Matrix Selection in the main body of this paper), but the applied loads are not as well matched to actual flight conditions as those of the triple-loads data set. This problem is being addressed in subsequent calibrations by applying a wider variety of triple loads (ref. 5).

The performances of the triple-loads and double-plus-triple-loads calibration matrices are shown in figures D1 through D12; figures D13 through D18 show results for the geometric matrix for reference. In each figure, the predicted loads in each axis are plotted against a single applied load. The data are from the triple-loads data set, where lift ($Z$) and torque ($N$) are held constant at 50% of the full-scale loads listed in table 1. All data have been normalized and plotted as percentages of full-scale loads in the relevant axes. Perfect predictions would either follow the applied loads exactly (along the dashed diagonal reference lines), or be straight horizontal lines for zero or constant loads.

The geometric matrix predictions (figs. D13–D18) have both slope errors and zero-load biases. The double-plus-triple-loads matrix predictions (figs. D7–D12) show marked improvements in zero-load biases, and lesser improvements in slope. The triple-loads matrix predictions (figs. D1–D6) show further improvements in slope. In hover and straight-and-level flight, most steady loads ($X$, $Y$, $L$, and $M$) are relatively small. Moderate slope errors may, therefore, be tolerated as long as bias errors remain low. This is why the double-plus-triple-loads calibration matrix gives acceptable results. The improvements in slope error shown by the triple-loads matrix were not great enough to compensate for its inferior prediction of rotor shaft strain-gage torque, as discussed previously under Calibration Matrix Selection.

TABLE D1.– ROOT-MEAN-SQUARE ERRORS IN THE APPLIED-LOAD AXIS FOR A VARIETY OF MATRICES AND DATA SETS (HYSTERESIS EFFECTS ELIMINATED)

| Matrix (generative data set) | Axis (measurement and applied-load) | | | | | |
|---|---|---|---|---|---|---|
| | $X$, lb | $Y$, lb | $Z$, lb | $L$, ft-lb | $M$, ft-lb | $N$, ft-lb |
| | Errors for the single-loads data set | | | | | |
| Geometric | 51 | 157 | 163 | 251 | 268 | 84 |
| Single | 46 | 41 | 62 | 380 | 258 | 92 |
| Double | 99 | 112 | 335 | 822 | 1080 | 456 |
| Triple | 306 | 182 | 401 | 755 | 331 | 895 |
| Single + double | 95 | 124 | 282 | 615 | 838 | 385 |
| Double + triple | 106 | 103 | 344 | 832 | 974 | 771 |
| Single + double + triple | 101 | 116 | 293 | 616 | 754 | 696 |
| | Errors for the double-loads data set, averaged over all constant loads | | | | | |
| Geometric | 182 | 139 | 348 | 1043 | 1097 | 554 |
| Single | 158 | 122 | 380 | 891 | 1142 | 516 |
| Double | 135 | 67 | 94 | 583 | 522 | 291 |
| Triple | 287 | 195 | 82 | 1061 | 1279 | 1129 |
| Single + double | 134 | 67 | 149 | 617 | 527 | 307 |
| Double + triple | 127 | 67 | 95 | 597 | 616 | 341 |
| Single + double + triple | 128 | 66 | 150 | 621 | 609 | 319 |
| | Errors for the triple-loads data set | | | | | |
| Geometric | 247 | 302 | 451 | 637 | 745 | 864 |
| Single | 334 | 376 | 459 | 112 | 2357 | 834 |
| Double | 377 | 127 | 169 | 287 | 1050 | 455 |
| Triple | 295 | 30 | 58 | 134 | 193 | 383 |
| Single + double | 357 | 124 | 203 | 364 | 1175 | 497 |
| Double + triple | 323 | 103 | 169 | 303 | 336 | 407 |
| Single + double + triple | 321 | 105 | 202 | 328 | 460 | 380 |

TABLE D2.– ROOT-MEAN-SQUARE ERRORS AVERAGED OVER ALL APPLIED LOADS FOR A VARIETY OF MATRICES AND DATA SETS (HYSTERESIS ERRORS ELIMINATED)

| Matrix (generative data set) | Measurement axis | | | | | |
|---|---|---|---|---|---|---|
| | *X*, lb | *Y*, lb | *Z*, lb | *L*, ft-lb | *M*, ft-lb | *N*, ft-lb |
| | Errors for the single-loads data set | | | | | |
| Geometric | 114 | 81 | 143 | 358 | 666 | 251 |
| Single | 42 | 72 | 128 | 243 | 346 | 214 |
| Double | 75 | 81 | 342 | 572 | 1020 | 337 |
| Triple | 280 | 160 | 526 | 495 | 1035 | 1391 |
| Single + double | 66 | 68 | 267 | 497 | 810 | 303 |
| Double + triple | 72 | 87 | 343 | 572 | 1056 | 418 |
| Single + double + triple | 65 | 72 | 268 | 494 | 876 | 391 |
| | Errors for the double-loads data set, averaged over all constant loads | | | | | |
| Geometric | 239 | 149 | 304 | 932 | 1040 | 339 |
| Single | 166 | 132 | 331 | 899 | 1189 | 387 |
| Double | 124 | 68 | 68 | 558 | 457 | 203 |
| Triple | 329 | 214 | 195 | 911 | 1395 | 1350 |
| Single + double | 124 | 68 | 106 | 586 | 513 | 210 |
| Double + triple | 126 | 70 | 67 | 561 | 505 | 282 |
| Single + double + triple | 125 | 69 | 105 | 588 | 534 | 266 |
| | Errors for the triple-loads data set | | | | | |
| Geometric | 328 | 255 | 275 | 475 | 956 | 1565 |
| Single | 271 | 353 | 291 | 296 | 2431 | 1530 |
| Double | 289 | 89 | 73 | 236 | 1180 | 962 |
| Triple | 284 | 30 | 53 | 103 | 353 | 401 |
| Single + double | 282 | 86 | 82 | 212 | 1298 | 1037 |
| Double + triple | 275 | 57 | 73 | 210 | 589 | 508 |
| Single + double + triple | 274 | 58 | 82 | 204 | 685 | 564 |

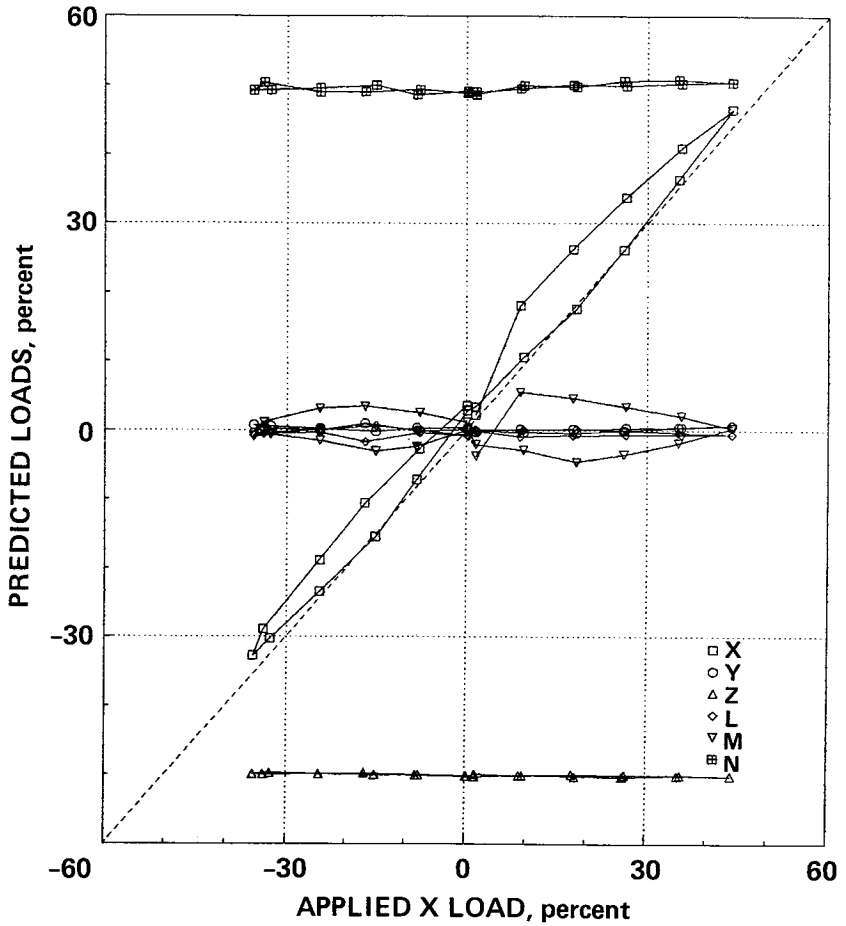


Figure D1.– Predicted loads versus applied X load using triple-loads matrix.

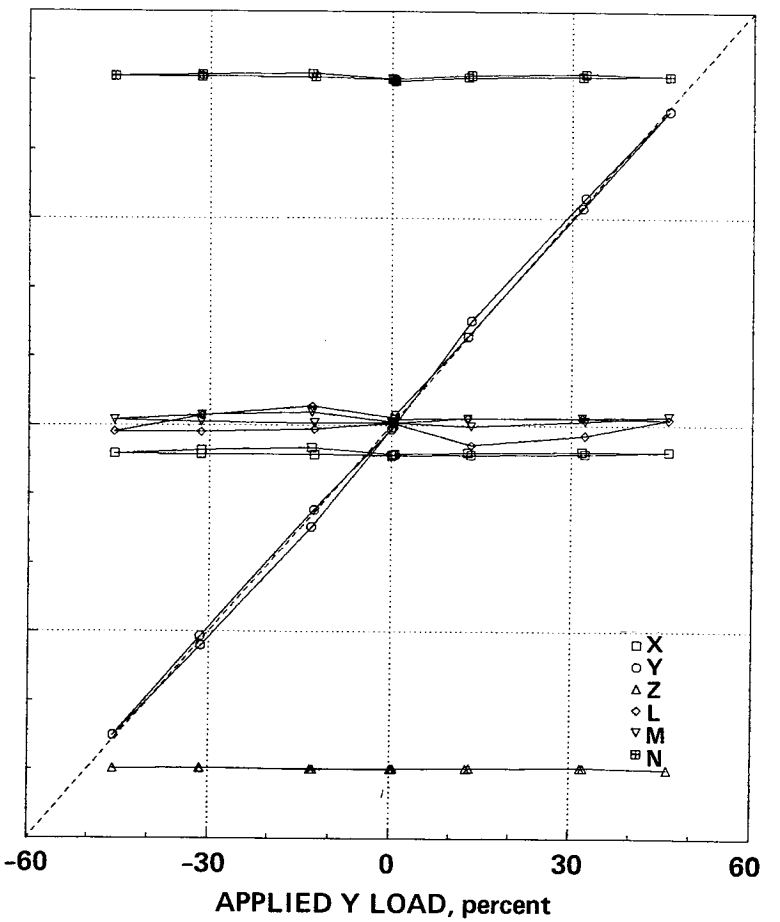


Figure D2.– Predicted loads versus applied Y load using triple-loads matrix.

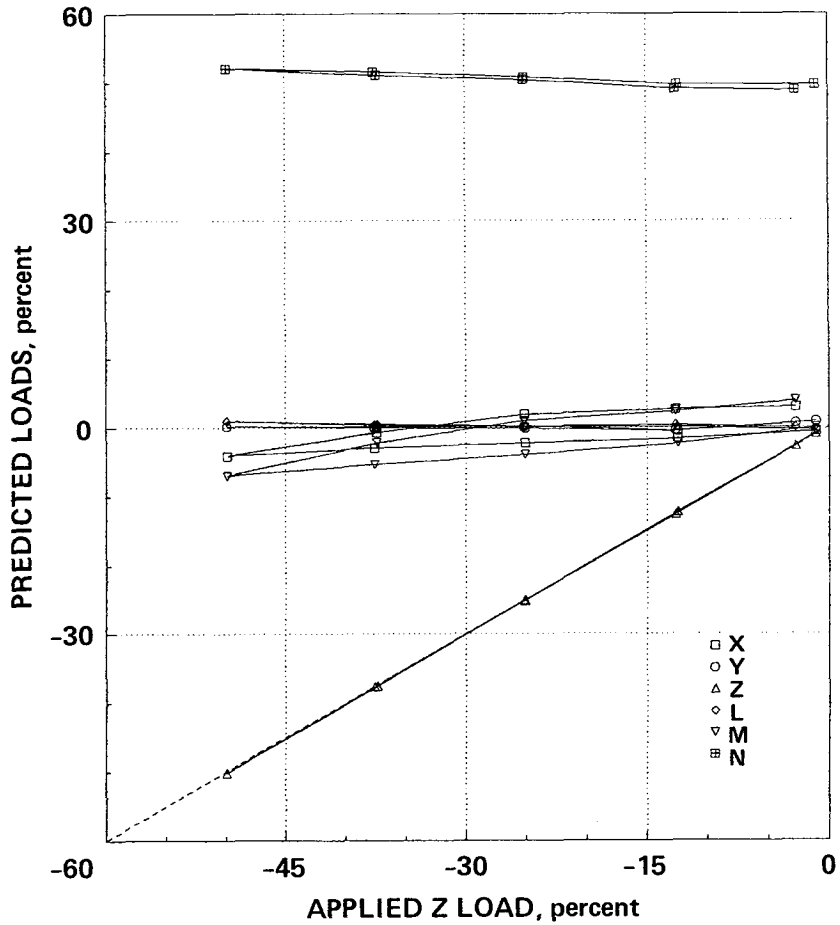


Figure D3.– Predicted loads versus applied Z load using triple-loads matrix.

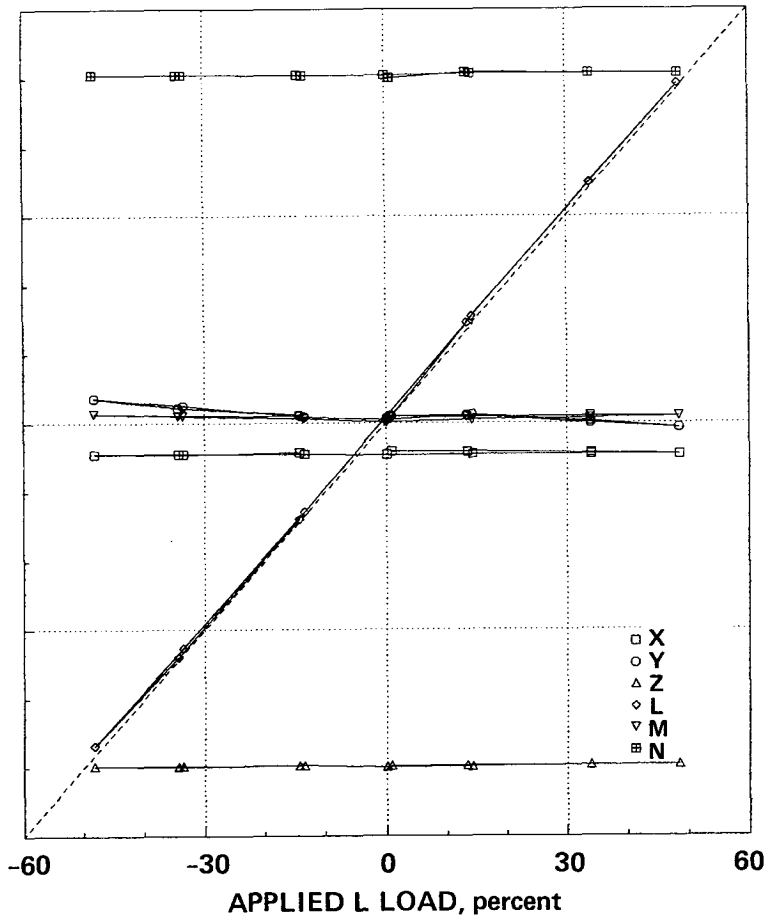


Figure D4.– Predicted loads versus applied L load using triple-loads matrix.

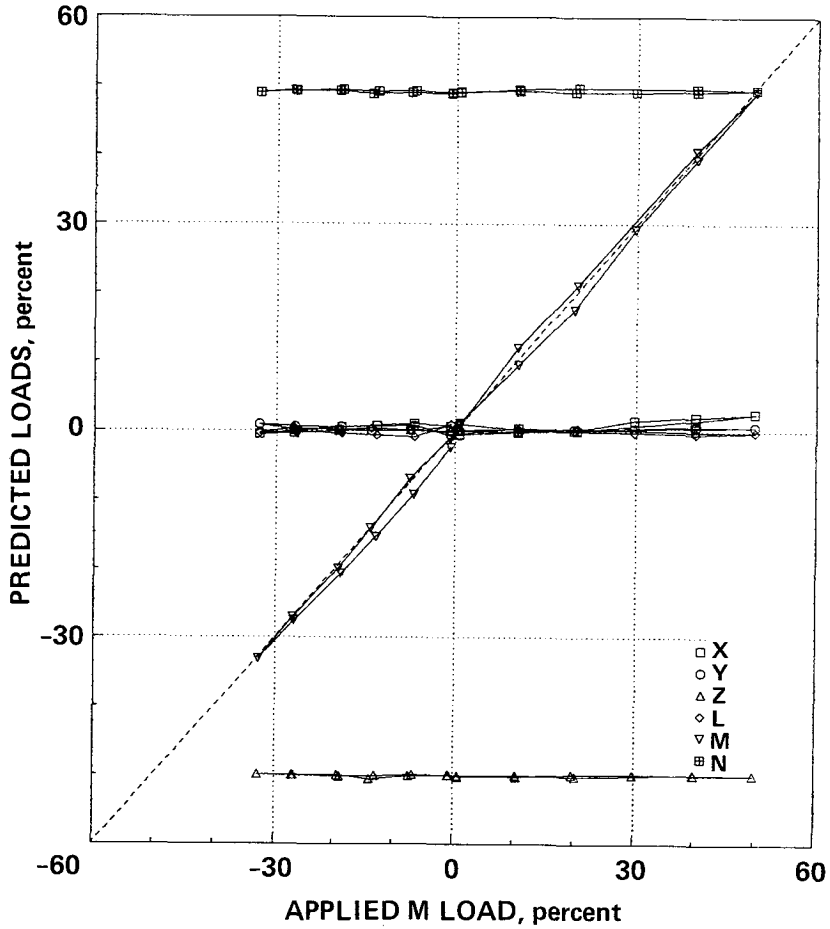


Figure D5.– Predicted loads versus applied M load using triple-loads matrix.

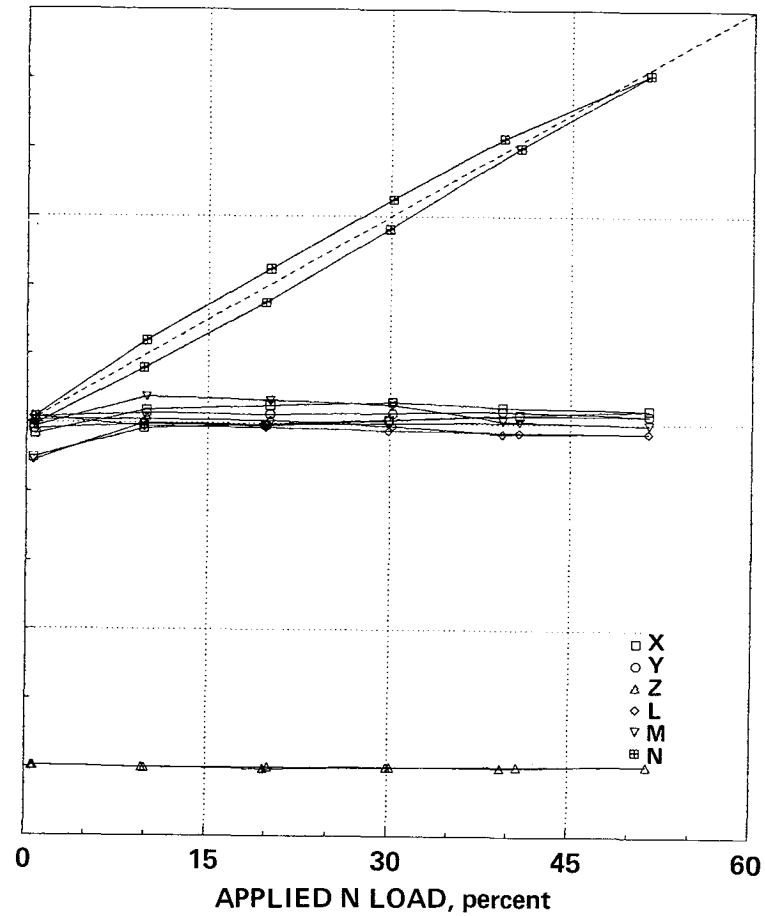


Figure D6.– Predicted loads versus applied N load using triple-loads matrix.

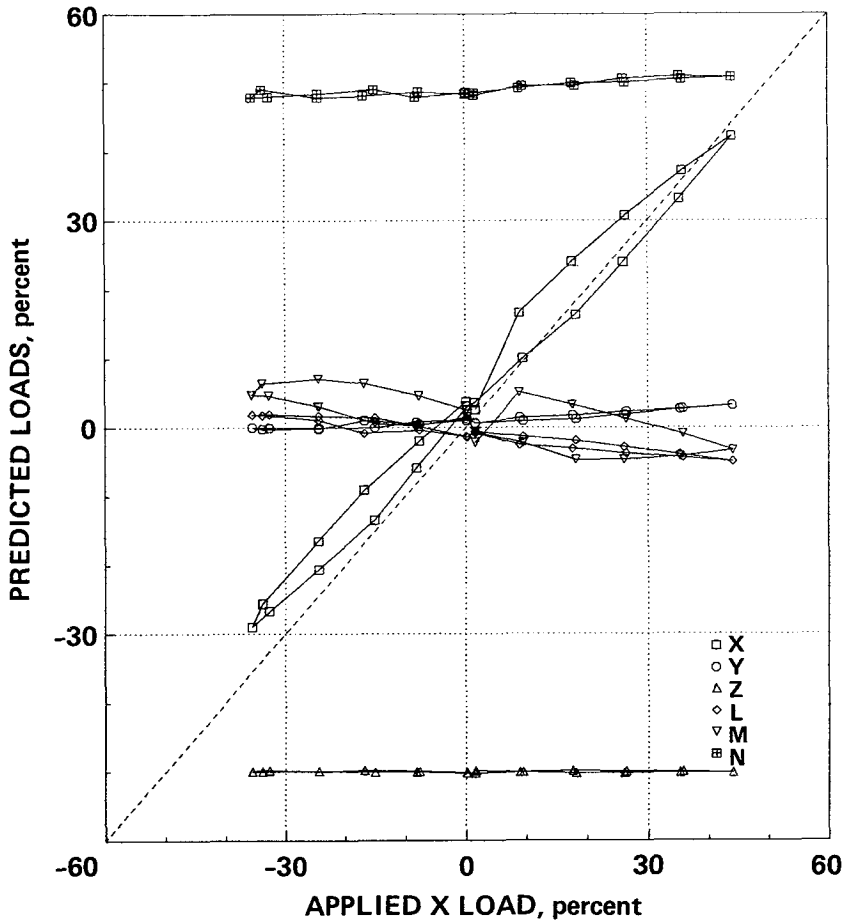


Figure D7.– Predicted loads versus applied X load using double-plus-triple-loads matrix.

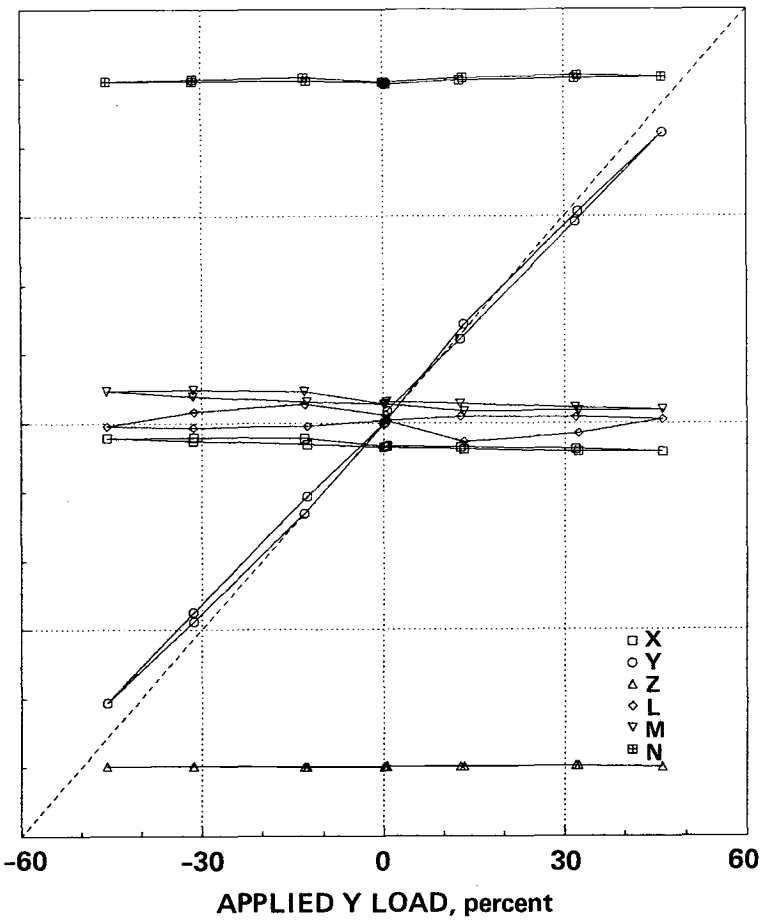


Figure D8.– Predicted loads versus applied Y load using double-plus-triple-loads matrix.

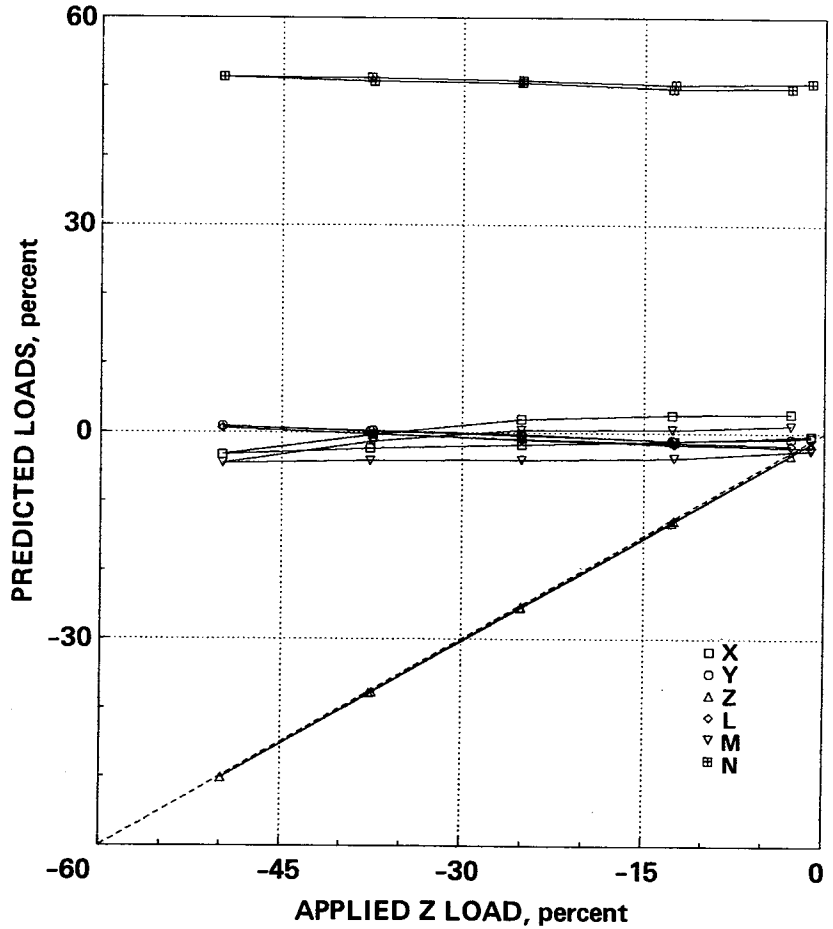


Figure D9.– Predicted loads versus applied Z load using double-plus-triple-loads matrix.

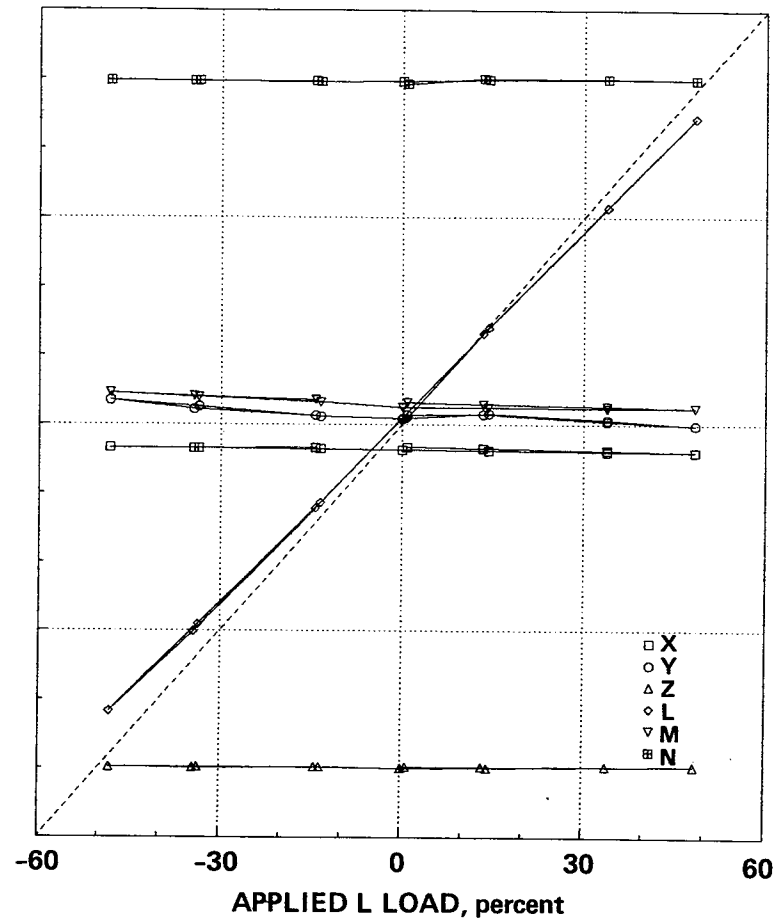


Figure D10.– Predicted loads versus applied L load using double-plus-triple-loads matrix.

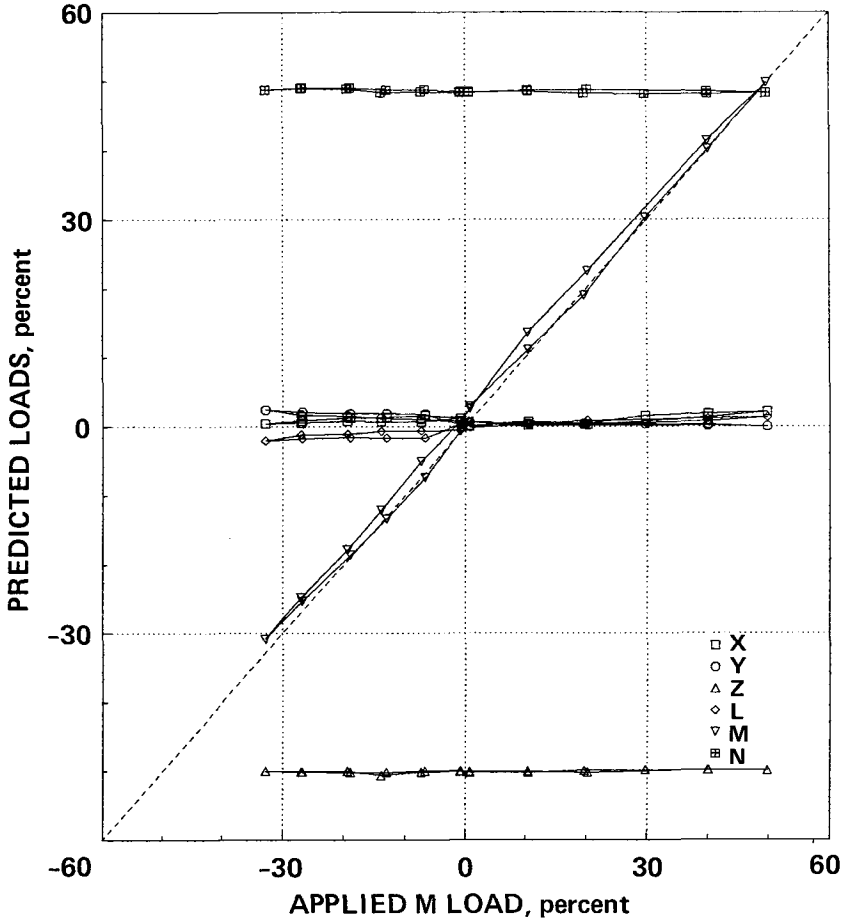


Figure D11.– Predicted loads versus applied M load using double-plus-triple-loads matrix.

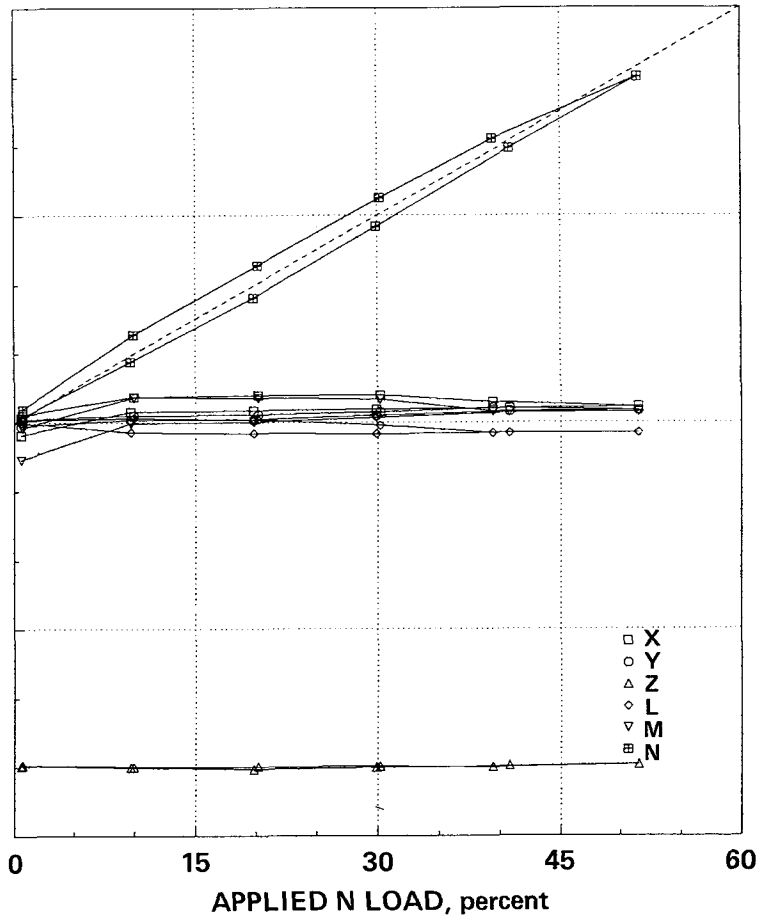


Figure D12.– Predicted loads versus applied N load using double-plus-triple-loads matrix.

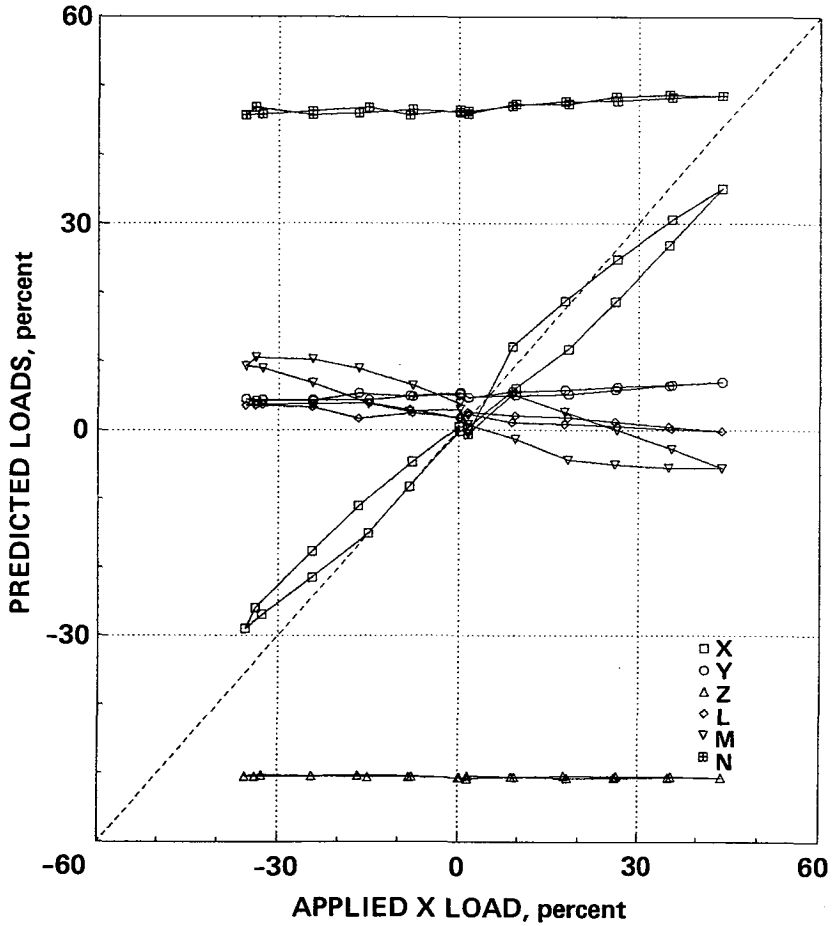


Figure D13.– Predicted loads versus applied X load using geometric matrix.

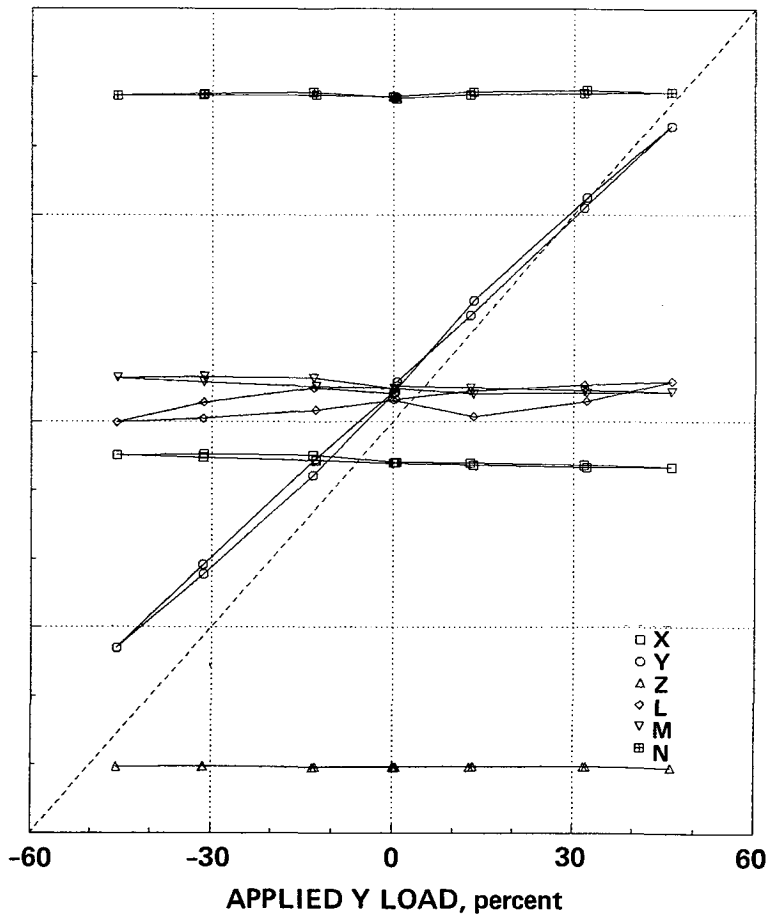


Figure D14.– Predicted loads versus applied Y load using geometric matrix.

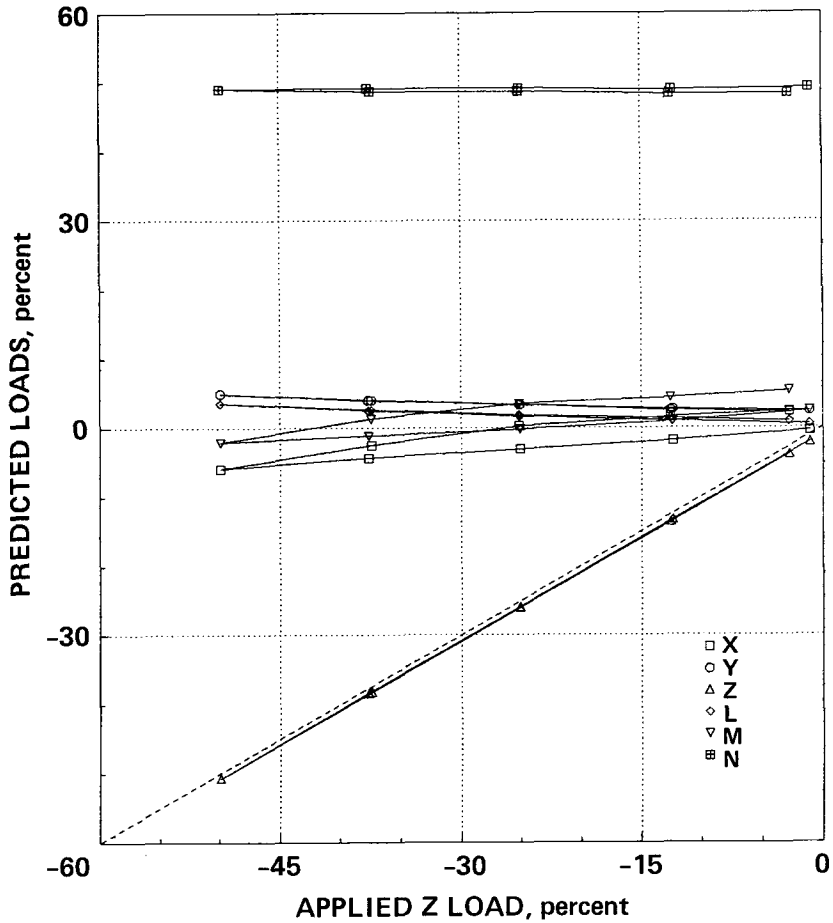


Figure D15.– Predicted loads versus applied Z load using geometric matrix.

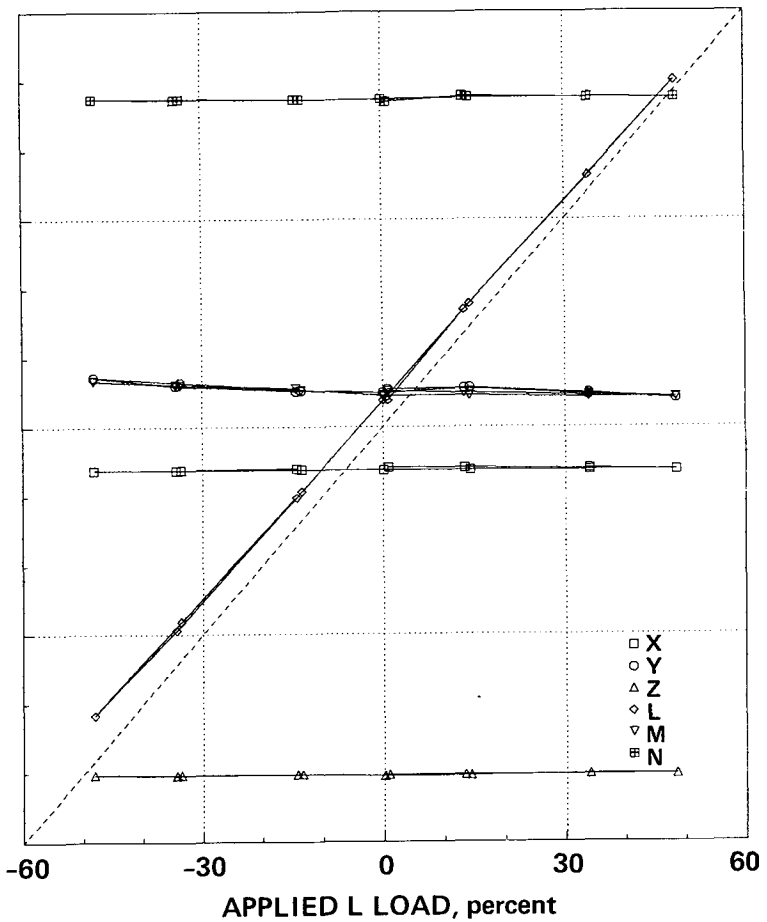


Figure D16.– Predicted loads versus applied L load using geometric matrix.

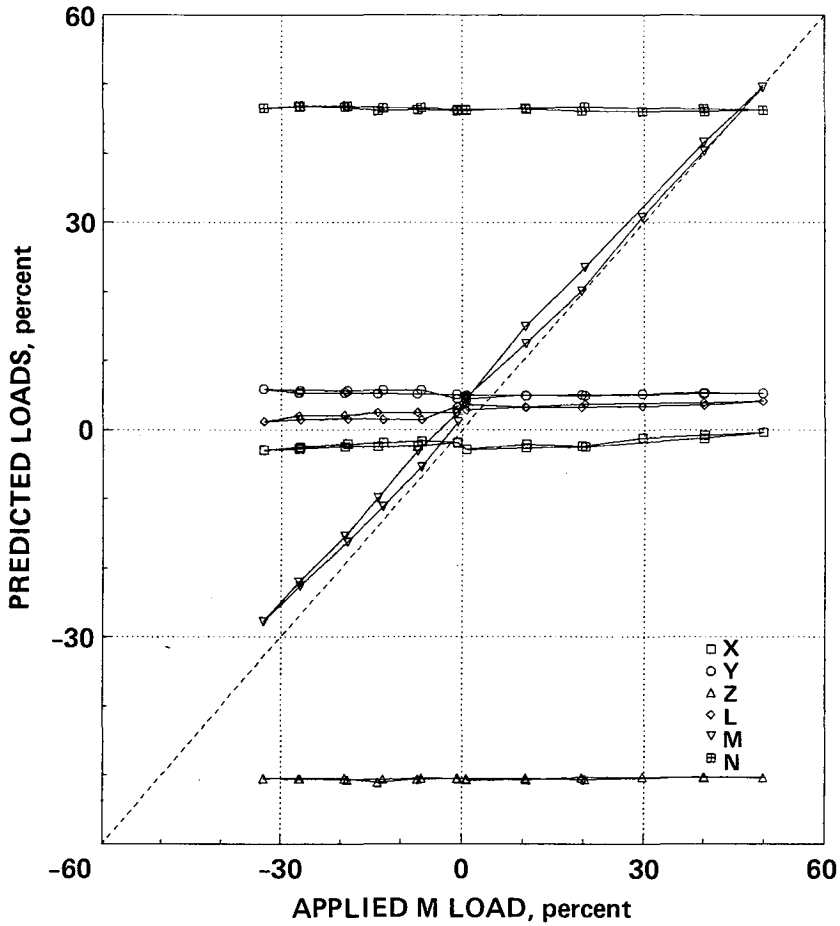


Figure D17.– Predicted loads versus applied M load using geometric matrix.

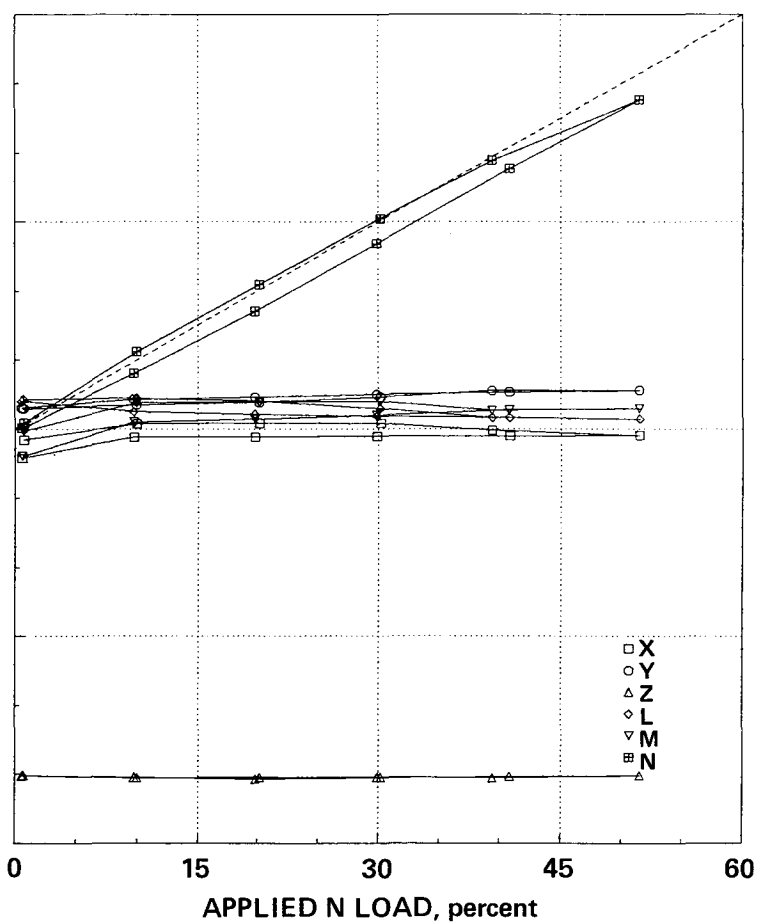


Figure D18.– Predicted loads versus applied N load using geometric matrix.

# REFERENCES


1. Flemming, R. J.; and Erickson, R. E.: An Evaluation of Vertical Drag and Ground Effect Using the RSRA Rotor Balance System. 38th Annual National Forum of the American Helicopter Society, Anaheim, Calif., May 1982.

2. Burks, J. S.: Rotor Systems Research Aircraft (RSRA) Rotor Force and Moment Measurement System. AIAA Paper 81-2516, Las Vegas, Nev., Nov. 1981.

3. Acree, C. W.: Performance of the Rotor Systems Research Aircraft Calibrated Rotor Loads Measurement System. 38th Annual National Forum of the American Helicopter Society, Anaheim, Calif., May 1982.

4. Acree, C. W. et al.: RSRA Static Calibration Facility Operations Manual. NASA TM-84389, 1983.

5. Acree, C. W.: Preliminary Results of the First Static Calibration of the RSRA Helicopter Active-Isolator Rotor Balance System. NASA TM-84395, 1983.

6. Jennrich, R. I.: Stepwise Regression. Statistical Methods for Digital Computers, chap. 4. K. Enslein, A. Ralston, and H. S. Nilf, eds., Wiley, New York, 1977.

7. Draper, N. R.; and Smith, H.: Applied Regression Analysis. Wiley, New York, 1966.

8. Condon, Gregory W.: Rotor Systems Research Aircraft (RSRA) Requirements for and Contributions to Rotorcraft State Estimation and Parameter Identification, AGARD Flight Mechanics Panel Specialists Meeting, Hampton, Va., Nov. 1974.

9. Crow, E. L.; Davis, F. A.; and Maxfield, M. W.: Statistics Manual. Section 3.1, Dover, New York, 1960.

10. Corro, J. J.: Error Analysis of the Measurement System for RSRA. Report SER-72001, Sikorsky Aircraft, Division of United Technologies Corporation, Stratford, Conn., Nov. 1973.

11. Monteleone, R. A.: Systems Requirements Handbook for the Rotor Systems Research Aircraft. Report SER-72039, Sikorsky Aircraft, Division of United Technologies Corporation, Stratford, Conn., Mar. 1977.

| 1. Report No. | 2. Government Accession No. | 3. Recipient's Catalog No. |
|---|---|---|
| NASA TP-2327 | | |

| 4. Title and Subtitle | 5. Report Date |
|---|---|
| RESULTS OF THE FIRST COMPLETE STATIC CALIBRATION OF THE RSRA ROTOR-LOAD-MEASUREMENT SYSTEM | August 1984 |
| | 6. Performing Organization Code: ATP |
| 7. Author(s): C. W. Acree, Jr. | 8. Performing Organization Report No.: A-9593 |
| | 10. Work Unit No.: T-3492 |
| 9. Performing Organization Name and Address: Ames Research Center, Moffett Field, California 94035 | 11. Contract or Grant No. |
| | 13. Type of Report and Period Covered: Technical Paper |
| 12. Sponsoring Agency Name and Address: National Aeronautics and Space Administration, Washington, DC 20546 | 14. Sponsoring Agency Code: 532-03-11 |

15. Supplementary Notes

Point of contact: C. W. Acree, Jr., Ames Research Center, MS 237-3, Moffett Field, CA (415) 965-6574 or FTS 448-6574

16. Abstract

The compound Rotor System Research Aircraft (RSRA) is designed to make high-accuracy, simultaneous measurements of all rotor forces and moments in flight. Physical calibration of the rotor force- and moment-measurement system when installed in the aircraft is required to account for known errors and to ensure that measurement-system accuracy is traceable to the National Bureau of Standards. The first static calibration and associated analysis have been completed with good results. Hysteresis was a potential cause of static calibration errors, but was found to be negligible in flight compared to full-scale loads, and analytical methods have been devised to eliminate hysteresis effects on calibration data. Flight tests confirmed that the calibrated rotor-load-measurement system performs as expected in flight and that it can dependably make direct measurements of fuselage vertical drag in hover.

| 17. Key Words (Suggested by Author(s)) | 18. Distribution Statement |
|---|---|
| Rotor load measurement<br>Rotor systems research<br>Helicopter static calibration | Unclassified - Unlimited<br><br>Subject Category: 05 |

| 19. Security Classif. (of this report) | 20. Security Classif. (of this page) | 21. No. of Pages | 22. Price* |
|---|---|---|---|
| Unclassified | Unclassified | 57 | A04 |

*For sale by the National Technical Information Service, Springfield, Virginia 22161

NASA-Langley, 1984